Materials Research Bulletin 185 (2025) 113274

Contents lists available at ScienceDirect

Materials Research Bulletin

journal homepage: www.elsevier.com/locate/matresbu

Research Papers

Magnetic and thermo-responsive microparticles based on calcium phosphates with high potential to produce structures for bone regeneration and local hyperthermia

Tânia S.S. Carvalho [a,*], João H. Belo [b], João C.C. Abrantes [c], Manuel Bañobre-López [d], Diogo Lopes [a], Andrei V. Kovalevsky [a], A. Kaushal [d], João P. Araújo [b], Susana M. Olhero [a,1], Paula M.C. Torres [a,1]

[a] Department of Materials Engineering and Ceramics (DEMaC), CICECO-Aveiro Institute of Materials, University of Aveiro, 3810-193 Aveiro, Portugal
[b] Institute of Physics of Advanced Materials, Nanotechnology and Photonics (IFIMUP), Department of Physics and Astronomy, University of Porto, 4169-007 Porto, Portugal
[c] ProMetheus, Polytechnic Institute of Viana do Castelo, 4900-347 Viana do Castelo, Portugal
[d] Advanced (Magnetic) Theranostic Nanostructures Lab, International Iberian Nanotechnology Laboratory (INL), Av. Mestre José Veiga s/n, 4715-330 Braga, Portugal

ARTICLE INFO

Keywords:
Iron-doped calcium phosphates
Hydroxyapatite
Magnetic properties
Hyperthermia
Bone regeneration

ABSTRACT

Magnetic calcium phosphate (CaP) nanoparticles have been explored for a wide range of applications, namely biodevices for bone regeneration and local cancer treating through hyperthermia therapy. Numerous shaping techniques to obtain dense and porous ceramic structures are based on colloidal processing principles, in which parameters such as crystallinity, morphology and particle size play an important role in obtaining high solids concentration suspensions to guarantee ceramic structures with high particle packing. With these considerations in mind, this work aims to obtain magnetic and thermo-responsive CaP microparticles, via wet chemical precipitation with the simultaneous addition of Fe^{2+} and Fe^{3+}. Magnetic microparticles with the ability to preserve their magnetic and magneto-thermal properties have been successfully achieved, due to the presence of well-distributed iron oxide nanocrystallites surrounded by CaP phases. This accomplishment promises great potential for the development of biodevices based on colloidal processing, as some Additive Manufacturing technologies.

1. Introduction

Magnetic calcium phosphates (CaP) mainly focused on magnetic hydroxyapatite (MHA, $Ca_{10}(PO_4)_6(OH)_2$), have attracted considerable attention in the last years, due to their promising multifunctional applications in magnetic hyperthermia treatment, tissue engineering and bone regeneration [1–5]. Advances in scaffold design, particularly through additive manufacturing (AM) technologies, have highlighted the potential for polymer-based bone scaffolds in regenerative applications, providing context for the development of polymer-based magnetic composites that could similarly be used in scaffold fabrication or scaffold coating [6,7]. Besides those, controlled drug/gene delivery and antimicrobial activity, heavy metals and toxic dyes removal, biosensors, and development of contrast agents for magnetic resonance imaging, have been mentioned as other functionalities where MHA can have great potential [8–14].

The synthesis of MHA can be achieved through different techniques, being chemical precipitation, hydrothermal, sol-gel, mechanochemical and emulsion synthesis the most commonly explored [5]. The synthesis route and conditions used considerably influence the structural [9], and consequently, the magnetic and magnetothermal behaviour – crucial for their magnetic hyperthermia performance - of the resulting materials. The magnetic properties in CaP materials are achieved by typically loading magnetic nanoparticles (MNP) or HA particles with a magnetic core [8,15] or nanocomposites [7,16–20] as blends of HA. Crystalline iron oxides such as maghemite (γ-Fe_2O_3) or magnetite (Fe_3O_4) are the most commonly used MNP due to their superparamagnetic properties [21–23]. Although multiple previous studies have demonstrated

* Corresponding author.
E-mail address: tssc@ua.pt (T.S.S. Carvalho).
[1] Co-last authorship.

https://doi.org/10.1016/j.materresbull.2024.113274
Received 28 August 2024; Received in revised form 18 December 2024; Accepted 19 December 2024
Available online 22 December 2024

biocompatibility and non-toxicity of these magnetic nanocomposites in the short/medium period [16], the long-term effects of MNP remain controversial [24,25], motivating the search for alternatives [26,27], particularly for applications in bone tissue engineering.

In this context, doping β-tricalcium phosphate (β-TCP, β-$Ca_3(PO_4)_2$) and HA particles with transition metal ions capable of conferring intrinsic magnetic properties to the resulting materials has been explored [10,28–34]. Manganese, cobalt, zinc, copper, and iron [35,36], single or co-doped, are examples of ions used to provide HA or β-TCP with magnetic properties. In addition to magnetism, the chemical modification of calcium phosphates induced by these ions can improve physicochemical, mechanical, and anti-bacterial properties, thereby enhancing their biological performance [37,38]. In the particular case of Fe, it plays a key role in several bone metabolic processes like oxygen transport, deoxyribonucleic acid synthesis and electron transfer (energy metabolism) at physiological pH [39].

Superparamagnetic behaviour is cited in literature as the most suitable magnetic behaviour for achieving magneto-thermal effects [40,41]. However, most of the reported works presented in the literature that aimed to develop doped β-TCP powders with magnetic behaviour and/or hyperthermia performance have attained paramagnetic, antiferromagnetic, or diamagnetic-like behaviours instead of superparamagnetic [33,36]. For example, in Singh's work, β-TCP powders were doped with different concentrations of Fe^{3+}, ranging from 2.52 to 12.55 mol% [33]. The outcomes of this study demonstrated the ability of β-TCP to host 5.02 mol% of Fe^{3+} in its lattice leading to the formation of $Ca_9Fe(PO_4)_7$ and $CaFe_3(PO_4)_3O$ as crystalline phases when calcined at 900 °C. It was also verified that iron-doped β-TCP powders presented high crystallinity, biocompatibility, and hyperthermia performance, although the magnetization was not saturated even for high magnetic fields (10 kOe). Similar results have been reported by the same authors for Fe and Co co-substituted β-TCP [42]. Recently, Lauryna Sinusaite and co-authors [36] reported the structural, magnetic, mechanical, and biological properties of β−TCP co-doped with Fe^{3+} and Zn^{2+} ions in the range of 1–5 mol% by wet precipitation method. The authors concluded that powders annealed at 800 °C presented high crystallinity and paramagnetic behaviour, verifying that magnetization values were proportional to the content of dopant ions.

In contrast, when the target is iron doped HA, superparamagnetic-like behaviour was reported, mostly derived from the formation of magnetite particles as secondary phases [10,30,43]. Subha Balakrishnan and co-workers [43] used the hydrothermal method to synthesise iron doped HA without any further thermal treatment, showing that crystallite size, crystallinity, and lattice parameters decreased as the amount of Fe in HA samples increased. The saturation magnetizations reported were not higher than 0.029 emu g^{-1} for the maximum amount of iron studied (0.01 M of the precursor $Fe(NO_3)_3.9H_2O$)), without the presence of any magnetic secondary phases. Veerla et al. [10] synthesized hydroxyapatite nanoparticles (nHA) co-doped with Ag/Fe with controlled size. In this case, no thermal treatment was performed after chemical precipitation synthesis and iron oxides (such as magnetite) were detected as secondary phases for Ag/Fe doping concentrations. Aiming to minimize the formation of magnetite, Tampieri et al. [30] studied the potential to obtain intrinsic magnetism (superparamagnetic-like properties) and hyperthermia by doping HA with simultaneous addition of Fe^{2+} and Fe^{3+} ions, using a wet chemical precipitation method. The authors observed that powders calcined at a maximum temperature of 700 °C in Ar atmosphere exhibited low crystallinity and low thermal stability, resulting in the formation of Fe-containing β-TCP as the main phase, with a decrease of the magnetization values from 0.95 to 0.22 A m^2 Kg^{-1}. These results highlighted the influence of calcination temperature on the crystallinity and phases formed in the Fe doped CaP powders, which subsequently can impact their final performance. In fact, the powders' crystallinity and composition interfere with its degradation rate *in vitro* and *in vivo* [44], which in turn should influence the magnetic and magnetothermal performance over time. Moreover, these features also affect the powders processability, either by powder or colloidal-based technologies. Therefore, the development of magnetizable devices containing iron-doped CaP-based powders, with proper composition and crystallinity is crucial for simultaneous bone tissue regeneration and cancer treatment by a local magnetic hyperthermia application. To attain that, additional efforts are required to overcome the current difficulties and further contribute to the progress in this field.

Although nanometric particles have been extensively studied and show promising magnetic and magneto-thermal properties for magnetic hyperthermia treatments [5], micron-sized particles provide a smaller surface area, favourable for the development of highly concentrated inks for Direct Ink Writing (DIW) technologies [45,46]. The use of microparticles in these inks increases the packing density, facilitating the production of structurally strong structures with a high material loading [45,47]. The bigger particle size can also decrease the tendency for particle agglomeration, thereby tuning the rheological characteristics of the inks, crucial for ensuring the uniformity and accuracy of the extrusion-based additive manufacturing processes [45–48].

Given these challenges, there is an increased need for the development of biocompatible micron-sized, crystalline, and magnetically stable CaP-based materials with tuneable magnetic properties for simultaneous bone regeneration and local hyperthermia treatment. The present work aims to fill this gap, by exploring the most suitable processing conditions through a simple chemical precipitation approach. For this purpose, the influence of synthesis temperature, Fe content, and thermal treatment (calcination temperature) on the phase composition, crystallinity, size, morphology, magnetic and magneto-thermal properties of iron-doped CaP powders was investigated.

2. Experimental procedure

2.1. Synthesis and thermal treatment of calcium phosphate powders

Calcium phosphate powders doped with equimolar ratios of Fe^{2+} and Fe^{3+}, in total Fe ion concentrations of 10.82 mol% and 23.44 mol% relative to Ca ions, referred to as FeCaP1 and FeCaP2, respectively, were synthesized using an aqueous chemical precipitation method. Calcium hydroxide ($Ca(OH)_2$, ≥ 96 %, HoneyWell/FLUKA, Germany), phosphoric acid (H_3PO_4, 85 %, PanReac AppliChem, Barcelona, Spain), iron (II) chloride tetrahydrate ($FeCl_2.4H_2O$, HoneyWell/FLUKA, Germany) and iron (III) chloride hexahydrate ($FeCl_3.6H_2O$, HoneyWell/FLUKA, Germany) were used as chemical precursors for calcium, phosphorus, and iron, respectively. The precursors, consisting of a $Ca(OH)_2$ suspension containing iron ions and an H_3PO_4 solution were prepared using deionized water, while maintain a constant ($Ca + Fe^{2+} + Fe^{3+}$)/P molar ratio of 2.06. FeCaP1 was synthesised at two different temperatures (40 and 90 °C), while FeCaP2 was synthesised only at 40 °C. The mixture of the precursors resulted in a precipitated suspension, which was maintained under the following conditions: 1 h at the selected synthesis temperature under constant stirring (200 rpm) and a target pH of approximately 11, followed by a maturation period of 24 h at rest, maintaining the synthesis temperature. An appropriate amount of ammonium hydroxide (NH_4OH, 25 %, PanReac, AppliChem, Barcelona, Spain) was added to adjust and maintain the constant pH during the first hour of the synthesis reaction.

Additionally, for comparison purposes, another powder named RefFeCaP was synthesised using the same chemical precursors mentioned above, following the experimental procedure described by Tampieri et al. [30] but varying the (Ca+Fe)/P molar ratio, the total amount of iron and synthesis conditions, such as stirring and pH. Briefly, the precursors ($Ca(OH)_2$ suspension containing iron ions + H_3PO_4 solution) were prepared to have a ($Ca + Fe^{2+} + Fe^{3+}$)/P molar ratio of 2.02 and a total Fe ion concentration (Fe^{2+} and Fe^{3+} in equimolar ratio) of 19.79 mol% relative to Ca ions. The precipitated suspension was maintained at 40 °C for 3 h under constant stirring (700 rpm) and,

controlled pH (target pH≈12), followed by a maturation period of 24 h at room temperature (RT). The pH of the suspension during the first 3 h of synthesis was controlled by the addition of the required amount of NH_4OH solution. The resultant precipitates of all synthesis were separated through vacuum filtration, washed three times with deionized water and then dried at 110 °C overnight. The obtained powders were manually deagglomerated in a mortar and sieved through a 200 μm mesh.

To evaluate the effect of calcination temperature, the resulting synthesised powders were heat-treated in a tubular furnace (Termolab, Portugal) under an inert argon gas atmosphere (Ar ≥ 99.999 %, ALPHAGAZ™ 1 Ar, Algés, Portugal) at either 700 °C or 1000 °C, or only at 1000 °C, with a dwell time of 1 h.

Table 1 presents the sample codes (X-S-T) and (RefFeCaP-T) of the developed CaP powders, which were adopted to simplify their identification. In these codes, X refers to FeCaP1 or FeCaP2 powders with different planned molar concentrations of Fe (mol%); S stands for synthesis temperature (40 °C and 90 °C) and T represents the calcination temperature (700 °C and 1000 °C) or indicates no calcination (NC). RefFeCaP refers to the powder used in this work for comparison purposes, synthetised at the same thermal conditions described by Tampieri et al. [30], as detailed in the legend of Table 1. For example, FeCaP1–40–1000 denotes the CaP powder doped with 10.82 mol% of Fe, synthetized at 40 °C and calcined at 1000 °C.

Fig. 1 presents a schematic representation of the experimental procedure of the synthesis and thermal treatments of the developed CaP powders, as described above, along with the techniques used for their characterization, providing a clear overview of the steps and methodological sequence employed.

After calcination at 1000 °C under an inert atmosphere, the FeCaP1–40–1000, FeCaP2–40–1000, and RefFeCaP-1000 powders were subjected to a second heat treatment in air at 600 °C for 1 h. These samples are referred to as FeCaP1–40–1000–600, FeCaP2–40–1000–600 and RefFeCaP-1000–600, respectively. This additional treatment was performed to evaluate the effect of an oxidising atmosphere on the phase composition of these powders.

2.2. Characterization methodology

2.2.1. Diffraction and spectroscopic analysis

2.2.1.1. X-ray diffraction. Crystalline phase analysis of all powders was performed by X-ray powder diffraction (XRD), using a high resolution X'Pert PRO diffractometer (Malvern PANanalytical, Worcestershire, United Kingdom) with a CuKα (α=1.54060 Å, 45kV and 40 mA) radiation and a Ni monochromator. The data were acquired in a 2θ range 5-70° with a step size of 0.0260. Rietveld's refinement method was used to evaluate quantitative crystalline phase composition and cell parameters (TOPAS v. 5.0, Bruker AXS, Karlsruhe, Germany) of all samples.

To evaluate the presence and quantification of the amorphous phase, corundum (NIST SRM 676a) was added as an internal standard to the as-prepared FeCaP1–40 samples, as well as those calcined at 700 °C and 1000 °C under an inert atmosphere of Ar gas. The same procedure was followed for FeCaP1 synthetised at 90 °C and for the formulations containing higher iron content (FeCaP2 and RefFeCaP), but only those calcined at 1000 °C under inert atmosphere. These mixtures were ground in an agate mortar to homogenize the samples. The phase fractions obtained by Rietveld's refinements were rescaled based on the absolute mass of corundum added, and internally renormalised.

2.2.1.2. Infrared spectroscopy. XRD information was complemented with infrared spectra obtained by Fourier Transform Infrared Spectroscopy (FTIR) in the region between 4000–400 cm^{-1} (Bruker Tensor 27 FT-IR spectrometer, Massachusetts, USA). For this purpose, each powder was mixed with potassium bromide (KBr) in a mass ratio of 1/150 (m/m) and pressed into a pellet for 15 min. Each infrared spectrum was obtained by averaging 128 scans collected at a resolution of 4 cm^{-1} at room temperature.

2.2.1.3. ICP optical emission spectrometry. Inductively Coupled Plasma Optical Emission Spectrometry analysis (ICP-OES, Jobin Yvon Activa M., USA) was used to determine the overall content of Fe in each sample. For this purpose, the required amounts of powders were dissolved in nitric acid (HNO_3) prior to ICP analysis. The obtained values were expressed in weight percent of Fe (wt%).

2.2.2. Thermal analysis

The thermal behaviour of the as-prepared powders was analysed through the combined thermogravimetry (TG) and differential scanning calorimetry (DSC) analyses using the Simultaneous Thermal Analyser STA449 F3 Jupiter® (Netzsch, Germany) equipment. Samples of 31 - 58 mg of each synthesized powder were placed in alumina crucibles. All measurements were performed under an argon atmosphere, with an argon flow rate of 50 mL min^{-1}, from RT (~24 °C) to 1000 °C at two distinct heating rates: 5 K min^{-1} and 10 K min^{-1}. The results were normalized to mass to ensure consistency and eliminate any potential discrepancies due to variations between sample mass of the different powders.

2.2.3. Surface area, porosity, and density

Nitrogen adsorption/desorption isotherms measurements at 77 K have been carried out on a Micromeritics Gemini 2370 V5.00 (Norcross, USA) device, after degassing the powders overnight at 200 °C (Micromeritics Flow Prep 060, Norcross, USA). Specific surface areas (SSA) of the powders were determined by Brunauer-Emmet-Teller (BET) method. The pore volume and pore size distribution were determined from the desorption isotherm using the Barrett–Joyner–Halenda (BJH) method.

The true density of the powders was determined by the Anton Paar Ultrapyc 5000 Micro (Graz, Austria) helium pycnometer using samples with an approximate weight between 2 and 5 g previously dried

Table 1
Sample codes (X-S-T) and RefFeCaP-T of the studied Fe-doped CaP powders. In these codes, X = FeCaP1 or FeCaP2 depending on the planned total Fe concentrations; S = synthesis temperature (°C); T = calcination temperature (°C) or NC (*No Calcination*); RefFeCaP = reference powder used for comparison purposes and synthesised* at 40 °C during the first 3 h and then at RT.

Sample Code X-S-T/RefFeCaP	Planned molar concentration of total Fe (mol%)	Synthesis Temperature (°C) S	Calcination Temperature (°C) under an inert atmosphere T
FeCaP1–40-T	10.82	40	NC
			700
			1000
FeCaP1–90-T		90	NC
			700
			1000
FeCaP2–40-T	23.44	40	NC
			1000
RefFeCaP-T	19.79	-*	NC
			1000

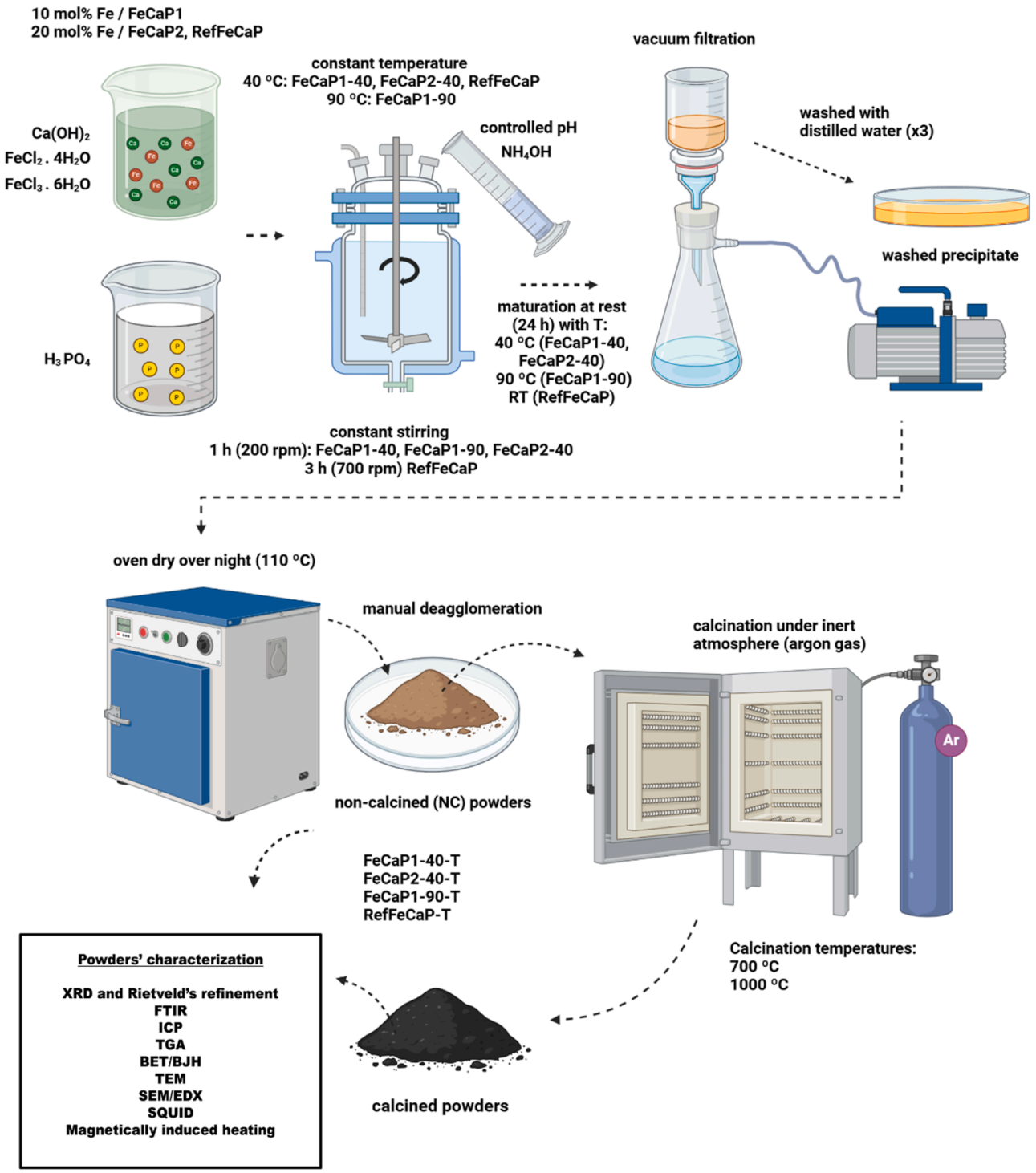

Fig. 1. Schematic representation of the synthesis method used to obtain the FeCaP powders and their respective characterization techniques. Created in BioRender. Carvalho, T. S. S. (2024).

overnight at 110 °C. The analyses were performed in a micro cell with a target pressure of 10 psi, at 25 °C, in a pulsed preparation mode.

2.2.4. *Morphological and microstructural characterization*

Transmission electron microscopy (TEM) analysis was performed with a HR-(EF) TEM JEOL 2200FS, operating at 200 kV. Samples were prepared by placing a drop of the particles suspended in ethanol onto a carbon-coated copper grid and allowing it to dry at room temperature.

The high-resolution images obtained from the selected samples were analysed in detail. The interatomic distances of the selected zones were measured to obtain the d-spacing values of crystalline structures, using the public domain DigitalMicrograph Software and by correspondence with (hkl) atomic planes obtained with XRD refinements and literature CIF files data. SEM imaging and EDX spectroscopy analysis were performed in a FEI Quanta 650 FEG scanning electron microscope operated at an accelerating voltage of 30 kV and a spot size of 3. Everhart-Thornley secondary electron detector was used for imaging and INCA X-Act X-Ray detector (Oxford Instruments) for EDX spectroscopy. Iron, Calcium and Phosphorus elemental maps were acquired for 15 min by using the corresponding Kα lines, 6.4, 3.7 and 2.0 keV, respectively.

Samples for SEM were prepared by depositing a small amount of powder on double-sided carbon tape attached to the aluminium SEM stub. No conductive coating was applied to the samples.

2.2.5. Magnetic characterization and hyperthermia capacity

Magnetic measurements were performed using a Quantum Design MPMS3 SQUID-VSM Magnetometer in the temperature range from 5 K up to 370 K and under magnetic fields up to ± 55 kOe. In this work, the magnetic moment of approximately 45 mg of powder was measured as a function of the magnetic field between -40 and 40 kOe at 300 K.

Measurements of magnetically induced heating were performed using a commercial magnetic hyperthermia equipment (Nanoscale Biomagnetics, Spain). Specifically, 0.100 g of each FeCaP powder specimen was suspended in 300 μL of deionized water. The measurements were conducted under alternating magnetic field (AMF) at frequencies of 268 kHz, 554 kHz, and 869 kHz, while subjected to a magnetic field intensity of 200 Oersted (Oe). An optical fibre-based thermometer was used to measure the temperature of the sample. Specific Absorption Rate (SAR) of FeCaP powders was calculated using the following equation:

$$SAR = ((\rho \cdot C_w) / m_{Fe}) \cdot (dT / dt) \quad (1)$$

where ρ is the density of the measured suspension (FeCaP powder + water), C_w is the specific heat capacity of water ($C_w = 4.185$ J g^{-1} K^{-1}) and m_{Fe} is the sample's mass used in the test normalised to the Fe contents of the analysed samples. The term dT/dt is the slope of temperature curve *versus* time at the initial time interval, obtained in the region where the SAR is considered adiabatic for a heterogeneous material.

3. Results and discussion

3.1. Influence of synthesis conditions and thermal treatment on phase composition and crystallinity

The effect of synthesis temperature (40 °C and 90 °C) on the XRD patterns of the FeCaP1 powders is presented in Fig. 2a, while the influence of calcination temperature under an inert atmosphere (NC, 700 °C and 1000 °C) on the powders synthesised at 40 °C (FeCaP1–40) is shown in the XRD patterns of Fig. 2b. Additionally, Fig. 2c and d compare the XRD patterns of powders with two different iron contents synthesised at 40 °C (FeCaP1 and FeCaP2) against the reference powder RefFeCaP (which has an iron content closer to FeCaP2), both non-calcined and after calcination at 1000 °C under an inert atmosphere, respectively. Fig. 2e summarises the quantitative crystalline phase composition of FeCaP1–40-NC, FeCaP1–40–700, and all different powders calcined at 1000 °C before and after post-thermal treatment in air at 600 °C, as obtained by Rietveld refinements. Additionally, Fig. 2f presents the quantitative phase composition including the amorphous phase of FeCaP1–40-NC, FeCaP1–40–700, and FeCaP1–40–1000, as well as FeCaP1–90, FeCaP2–40 and RefFeCaP calcined at 1000 °C.

The XRD patterns of the non-calcined FeCaP1 powders synthesised at the two different temperatures (40 and 90 °C, Fig. 2a) are very similar and show broadened peaks, denoting low crystallinity. HA phase can be detected as the main phase when compared with the standard Powder Diffraction Files (PDF) of HA (number 04–015–5048). Concurrently, there is evidence of a minor and relatively broad peak corresponding to the presence of magnetite (Fe_3O_4, $Fe^{2+}Fe_2^{3+}O_4$) in the powder synthesised at 40 °C (FeCaP1–40-NC) consistent with the most intense peak presented by PDF of Fe_3O_4 (number 04–011–5952). No other peaks from other iron oxide phases as secondary phases were observed in the XRD patterns of these uncalcined powders.

The quantitative phase analysis obtained by Rietveld refinement for these powders' precipitates (Fig. 2e and f) corroborate the presence of small quantities of Fe_3O_4 in FeCaP1 obtained at 40 °C (FeCaP1–40-NC) and the apparent absence of this phase at 90 °C (FeCaP1–90-NC). However, the identification of magnetite peaks brings with it some uncertainty. Differentiating magnetite and maghemite from each other is very difficult by XRD because both phases have the same cubic crystal structure and almost identical lattice parameters, leading to coincident XRD characteristic peaks [49–51]. Thus, it was not possible to specify with certainty whether the phase present is magnetite or maghemite, or a mixture of both. However, the Rietveld refinements point to the presence of magnetite, and due to that, this phase was assumed in the XRD diffractograms analyses.

Previous studies have shown that in the syntheses of powdered calcium phosphates by aqueous chemical precipitation method, the Ca/P molar ratio in the precipitate did not depend directly on the Ca/P molar ratio of the initial reagents [52–56]. In fact, the composition of the precipitate strongly depends on the synthesis parameters, being pH and temperature the most important parameters to control, without disregarding the rate and time of stirring, as well as the ripening time and temperature. Throughout the synthesis of FeCaP1, the experimental fluctuations of pH values recorded at 40 °C were closest to the planned value (pH = 11), ranging from 11 (initial pH) to 10.8 (final pH). At the increased synthesis temperature of 90 °C, pH control by addition of ammonia solution was less effective, ranging from 10.6 (initial pH) to 10.3 (final pH). Thus, a slight pH deviation to higher values and a lower synthesis temperature favoured the precipitation of a tiny fraction of magnetite in the FeCaP1–40-NC. Furthermore, the diffractograms of the FeCaP1-NC powders synthesised at 40 and 90 °C (Fig. 2a) suggest that the iron ions have preferentially entered the HA structure [30].

Upon calcination at 700 °C and 1000 °C under an inert atmosphere, an increased intensity and sharpness of the XRD peaks is observed, indicating an improvement in the powder crystallinity with temperature, as expected (Fig. 2b; Fig. 2c when compared with Fig. 2d). Furthermore, the calcination temperature plays a key role in the final powders' composition, as can be proved by the XRD diffractograms (Fig. 2b) of the FeCaP1–40 powder complemented with the results presented in Fig. 2e and f. As the calcination temperature increases under an inert atmosphere, the characteristic peaks of the magnetite phase (one peak visible at 700 °C and two peaks at 1000 °C) become more intense, revealing an increase of the fraction of this phase in the crystalline composition of FeCaP1–40. When calcined at 1000 °C, in addition to the characteristic peaks of HA and magnetite, which appear, respectively, as predominant and secondary (though minority) phases, characteristic peaks of the β-TCP phase emerge as a new secondary phase. β-TCP phase only appears at 1000 °C, since its crystallisation temperature is above 700 °C [52,57–59].

It is to be noted that the crystalline phase composition of all powders follows a similar trend as calcination temperature increases, regardless of the synthesis temperature used to produce them: the magnetite content increases, accompanied by a decrease of HA and the concomitant appearance of the β-TCP phase at 1000 °C (Fig. 2e). The FeCaP1 powders (FeCaP1–40 and FeCaP1–90) calcined at 1000 °C contain a similar amount of magnetite. However, the quantity of β-TCP present in their composition increases with higher synthesis temperatures, reaching around 40 wt% in the powder synthesised at 90 °C (FeCaP1–90–1000) (Fig. 2f), or almost 50 wt% considering only the crystalline fraction of the powder (Fig. 2e).

Doubling the iron amount in FeCaP1 and maintaining a synthesis temperature at 40 °C leads to obtaining the FeCaP2–40 powder that, in the uncalcined form, presents an XRD diffractogram with broader and less intense peaks (FeCaP2–40-NC, Fig. 2c) than the FeCaP1–40-NC. In addition, when calcined at 1000 °C, FeCaP2–40–1000 exhibits a similar magnetite content to FeCaP1–40–1000, but with β-TCP becoming the main phase instead of HA (around 63 wt% in Fig. 2f or 83 wt% considering only the crystalline fraction of the powder in Fig. 2e). The lower pH values recorded during the synthesis of FeCaP2–40 (initial pH = 10.3 and final pH = 9) and the higher concentration of iron contributed to the difference in composition between these two powders

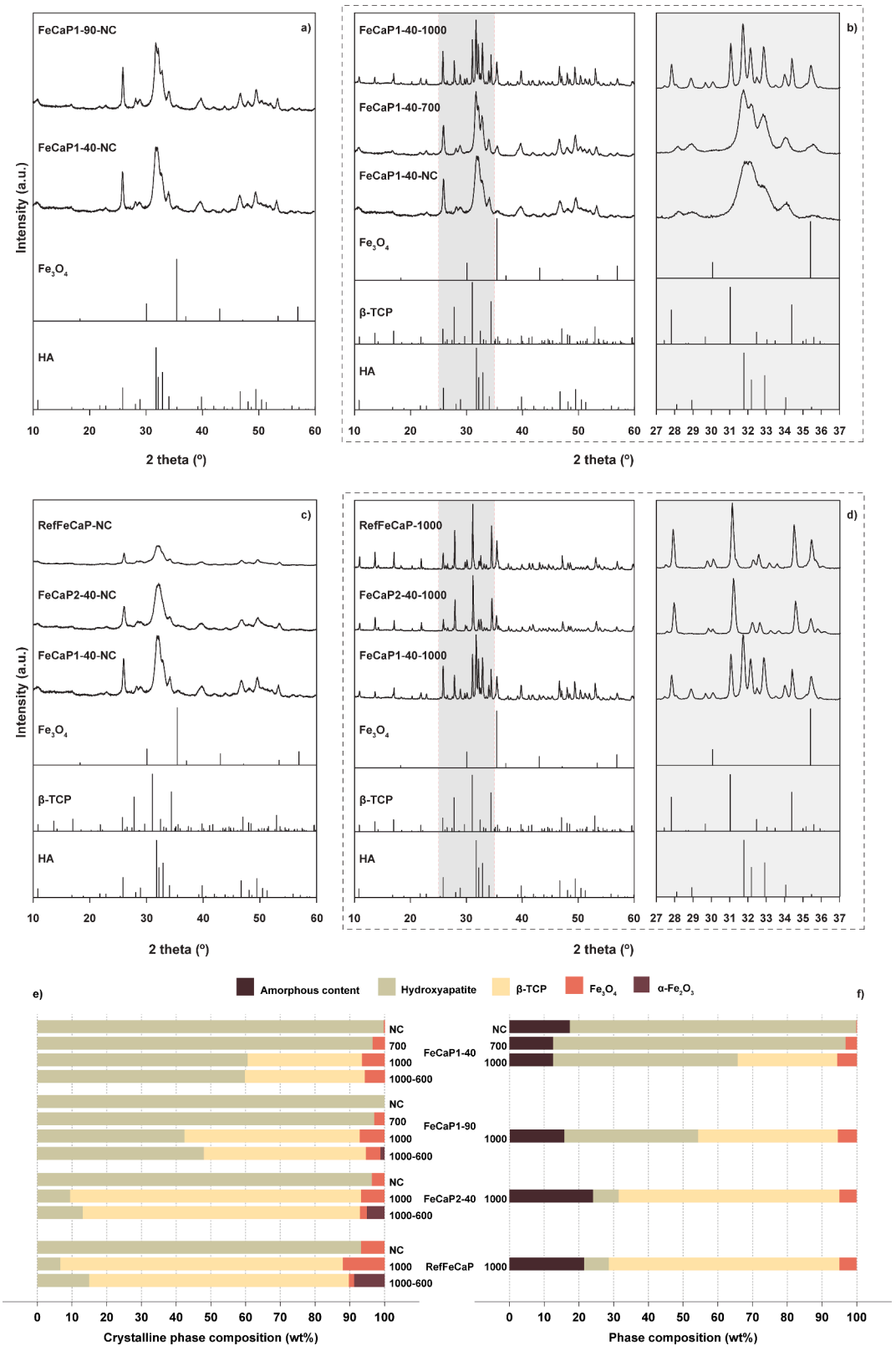

Fig. 2. X-ray diffractograms of: (a) FeCaP1-NC (Non-Calcined) synthetised at two different temperatures (40 °C and 90 °C); (b) FeCaP1 synthetised at 40 °C (FeCaP1–40) at different calcination temperatures (NC, 700 °C, 1000 °C) under an inert atmosphere, with zoomed area in the 2 theta range of 27–37°; (c) non-calcined FeCaP1–40-NC, FeCaP2–40-NC and RefFeCaP-NC, with different Fe content (lower in FeCaP1, see Table 1), and (d) these powders calcined at 1000 °C under an inert atmosphere, with zoomed area in the 2 theta range of 27–37°. The standard diffractograms of pure Fe_3O_4 (ICDD PDF number 04–011–5952), pure β-TCP (ICDD PDF number 04–006–9376) and pure HA (ICDD PDF number 04-015-7245) are also represented for comparison purposes. Quantitative analysis data obtained by Rietveld refinement of (e) crystalline phases compositions (wt%) of FeCaP1–40-NC, FeCaP1–40–700, and all the different powders calcined at 1000 °C under an inert atmosphere, before and after thermal treatment in air at 600 °C, and (f) phase composition of these powders including their amorphous phase.

Table 2
Quantity of magnetite Fe_3O_4 in weight percent (wt%) was quantified by Rietveld refinement for each sample, including the phase composition with the amorphous phase (Fig. 2f), along with the respective Fe content (Fe in Fe_3O_4). The repeatability limits (95 %) of the phase composition were assumed to be close to 1 % [65]. The total Fe content of each sample in wt% obtained from elemental ICP analysis. The quantity of Fe present in CaP (HA or β-TCP) as a substitution ion in the crystalline lattice was also determined.

Sample code	Fe_3O_4 (wt%) (± 1)	Fe in Fe_3O_4[a] (wt%) (± 1)	Total Fe[b] (wt%) (± 0.3)	Fe in CaP[c] (wt%) (± 1.3)
FeCaP1–40-NC	0.2	0.1		4.7
FeCaP1–40–700	3.3	2.4	4.8	2.4
FeCaP1–40–1000	5.7	4.1		0.7
FeCaP1–90–1000	5.5	4.0	4.8	0.8
FeCaP2–40–1000	5.0	3.6	9.8	6.2
RefFeCaP-1000	4.0	2.9	9.8	6.9

[a] Fe percentage in Fe_3O_4 by Rietveld's quantification (%Fe in Fe_3O_4 = (3·Mw (Fe) / Mw (Fe_3O_4)) · %Fe_3O_4 (Rietveld))
[b] Fe percentage calculated by ICP analysis
[c] Fe percentage in CaP (%Fe in CaP = %Fe (ICP) - %Fe in Fe_3O_4)

calcined at 1000 °C, since the other synthesis parameters remained constant. The diffractograms of RefFeCaP at 1000 °C (Fig. 2c and d) show the same trend as FeCaP2–40–1000, but with slightly higher magnetite and β-TCP contents (Fig. 2e) and lower HA phase, exhibiting the characteristic peaks of the magnetite and β-TCP phases slightly more intense. The origin of the differences in the compositions of these powders with identical Fe molar concentration (Table 1) can be found in the variation of the synthesis parameters. Comparing the synthesis of FeCaP2–40 and RefFeCaP, the latter showed a greater fluctuation in pH values (initial pH = 12.0 and final pH = 7.23), a higher rate and time of stirring, and the maturation period was carried out at room temperature. In both syntheses with higher Fe content (FeCaP2–40 and RefFeCaP), there is a more noticeable decrease in pH values throughout the process, reaching final pH values lower than those measured for FeCaP1. This more pronounced pH decrease could lead to a higher oxidation of the magnetite, forming maghemite and/or the coexistence of both magnetite and maghemite [60].

In the Fig. 2d, a small peak at 32.2° is noted in FeCaP2–40–1000 and RefFeCaP-1000, less intense for RefFeCaP-1000, which corresponds to the third most intense characteristic peak of the XRD pattern of pure HA (ICDD number 04–015–7245). If this peak corresponds to the characteristic XRD peak of the HA phase, the XRD peak at 32.2° becomes the most intense instead of the peak at 31.78° (211), indicating the existence of a preferential orientation in the (112) plane and the presence of a small quantity of this phase (Fig. 2d and e). A slight shift of β-TCP peaks to higher 2θ angles in XRD patterns of FeCaP2–40–1000 and RefFeCaP-1000 (zoomed area in Fig. 2d), was also observed, indicating that the lattice parameters of β-TCP tend to decrease with the incorporation of iron ions into its crystal lattice.

When analysing the composition of the crystalline fraction of the powders, together with their overall composition (Fig. 2f), including the existing amorphous fraction, RefFeCaP-1000 still contains a slightly higher β-TCP content, with similar quantities of HA (~ 7 wt%), and a slightly lower content of amorphous phase and magnetite compared to the FeCaP2-40-1000 powder composition. Interestingly, these powders with higher iron content (RefFeCaP-1000 and FeCaP2-40-1000) appear to have a higher amount of amorphous phase and, consequently, show a lower fraction of crystalline phases than FeCaP1 powders, as well as slightly lower magnetite contents (Fig. 2f).

The HA and β-TCP mixture achieved at 1000 °C and the increasing magnetite fraction with higher calcination temperatures indicate that the precipitated amorphous hydroxyapatites (uncalcined powders) from the different syntheses are calcium-deficient hydroxyapatites with (Ca+Fe)/P < 1.67. Thus, small variations in the (Ca+Fe)/P ratio of the precipitate resulting from synthesis conditions can lead to high variabilities in the powders' composition after calcination [52,53,55,56,58,59].

To evaluate if iron-doped phases and/or iron oxide species are stable when subjected to an oxidizing atmosphere, the FeCaP-1000 powders post-treated at 600 °C in air (FeCaP1-40-1000-600, FeCaP2–40–1000–600, and RefFeCaP-1000–600) were characterized by XRD (**Figure S1**), with the respective quantification of crystalline phases performed by Rietveld refinement (Fig. 2e). As stated in the literature, under oxidizing conditions, magnetite transforms into maghemite (γ-Fe_2O_3) at ≥ 200 °C, which in turn transforms into hematite (α-Fe_2O_3) within the temperature range of 350 to 600 °C [61–64]. These transformations occur because of the gradual oxidation of iron ions and the rearranging of the crystal lattice from an inverse spinel-like arrangement to a rhombohedral one [64]. Therefore, the subsequent thermal treatment of the powders in an oxidizing atmosphere at 600 °C reveals the presence of hematite (Fig. 2e), specifically in powders with higher iron content (FeCaP2–40–1000–600 and RefFeCaP-1000–600), in good agreement with the above considerations. Notably, this transition was very limited in the case of FeCaP1–90–1000–600 (around 1 wt% of the hematite phase) and not observed in the case of FeCaP1–40–1000–600, which exhibited a sustained presence of magnetite content, as well as HA and β-TCP phases. This result indicates that, in these powders, the magnetite might be embedded into the CaP matrix, protecting it from being converted into hematite.

From the results of the Rietveld refinement on the quantification of magnetite (phase composition including amorphous phase, Fig. 2f) and the total quantity of iron in each powder obtained by ICP (Table 2), it was possible to estimate the iron content present in the crystal structures of the CaP phases (HA or HA + β-TCP) as doping ion.

From ICP analysis, RefFeCaP-1000 and FeCaP2–40–1000 have the same Fe content (9.8 ± 0.03 wt%), which is incorporated in the crystalline structure of CaP phases, with the remainder in the form of magnetite. However, the RefFeCaP-1000 powder has a lower magnetite content than FeCaP2–40–1000 powder, suggesting a higher incorporation of Fe (~70 % of the total Fe amount) into the structure of CaP for RefFeCaP-1000. For FeCaP1–40, an increase in calcination temperature results in decreased Fe incorporation within the crystalline structure of the CaP phase and a corresponding increase in the magnetite content. This trend is consistent across all the other powders synthesised under various temperature conditions and Fe contents (data not shown). The results for all the FeCaP1 powders (FeCaP1–40 and FeCaP1–90) calcined at 1000 °C indicate a very low incorporation of Fe ions in the crystal structure of the CaP phases, with almost all Fe existing in the form of magnetite (Table 2). This is supported by the absence of β-TCP peak shifts to higher 2θ angles in the XRD pattern of these powders, which contrasts with the shifts observed in FeCaP2–40–1000 and RefFeCaP powders (zoom in Fig. 2d).

The refined lattice parameters of the HA and β-TCP structures of all powders (synthesised at 40 °C and 90 °C, and subsequently calcined at 700 °C and/or 1000 °C under an inert atmosphere Table 1) are displayed in Table 3. Cell parameters of the β-TCP structure were only refined in powders calcined at 1000 °C, since this phase is only detected in all powders at this calcination temperature.

Table 3 shows an increase in the unit cell volume of HA as calcination temperature increases for all powders, regardless of the synthesis

Table 3
Refined lattice *a*- and *c*- axis parameters, and unit cell volume of HA and β-TCP crystalline phases of Fe-doped calcium phosphate powders, are presented for different synthesis and calcination temperatures. For comparison, the standard values from ICDD 04–015–7245 for pure HA [66] and ICDD 04–006–9376 for pure β-TCP [67] are also included.

	Refined structural parameters					
	HA ($Ca_{10}(PO_4)_6(OH)_2$)			**β-TCP ($Ca_3(PO_4)_2$)**		
Sample	*a*-axis (Å)	*c*-axis (Å)	Cell Vol. (Å^3)	*a*-axis (Å)	*c*-axis (Å)	Cell Vol. (Å^3)
ICDD 04–015–7245	9.418	6.884	528.83	-	-	-
ICDD 04–006–9376	-	-	-	10.420	37.400	3516.720
FeCaP1–40-NC	9.424	6.868	528.240	-	-	-
FeCaP1–40–700	9.434	6.870	529.516	-	-	-
FeCaP1–40–1000	9.430	6.892	530.761	10.413	37.328	3505.235
FeCaP1–90-NC	9.427	6.864	528.253	-	-	-
FeCaP1–90–1000	9.464	6.870	532.889	10.414	37.327	3505.814
FeCaP2–40-NC	9.428	6.835	526.133	-	-	-
FeCaP2–40–1000	9.614	6.785	543.111	10.356	37.176	3452.847
RefFeCaP-NC	9.409	6.830	523.631	-	-	-
RefFeCaP-1000	9.605	6.791	542.574	10.392	37.304	3488.866

temperature conditions (40 or 90 °C) and the total Fe content (Table 2), but more evident for the FeCaP2–40 and RefFeCaP powders. For the FeCaP1 compositions, both lattice parameters along *a*-axis and *c*-axis of HA structure tend to increase with increasing calcination temperature. In the compositions with double of iron content (FeCaP2–40 and RefFeCaP), the lattice parameters along the *a*-axis and *c*-axis do not follow the same trend, being observed a clear increase along the *a*-axis and a decrease along the *c*-axis. In addition, these powders calcined at 1000 °C present higher *a*-axis and lower *c*-axis values of the HA structure comparatively to respective lattice parameter values of the standard HA (ICDD number 04–015–7245) and the FeCaP1 powders calcinated at 1000 °C (Table 3). Concerning the β-TCP lattice, the *a*-axis and *c*-axis parameters appear to be similar for the FeCaP1 compositions calcined at 1000 °C, irrespective of the synthesis temperature conditions (40 or 90 °C). For FeCaP2–40–1000 and RefFeCaP-1000, both the lattice parameters along the *a*-axis and *c*-axis of this structure (and consequently the volume of its unit cell) are lower than FeCaP1-40–1000 and FeCaP1-90–1000. In agreement with previous works [30,68] and consistent with the lower ionic radii of Fe^{2+} (0.78 Å) or Fe^{3+} (0.64 Å) in comparison to Ca^{2+} (1.00 Å), these results indicate that these powders incorporated more Fe into CaP lattice than FeCaP1–40–1000 and FeCaP1–90–1000, and their highest values of *a*-axis in HA lattice suggest the presence of oxyhydroxyapatite [64].

Fig. 3 shows the FT-IR results of the FeCaP powders synthesised at 40 °C at different calcination temperatures (non-calcined, 700 °C and 1000 °C). Wavenumbers and the assignments of the bands and peaks are summarised in Table 4.

Vibration modes in the range of 600–1120 cm^{-1} are assigned to phosphate groups from calcium phosphate-based crystalline phases [57, 69–72], while IR bands at ~630 cm^{-1} can be ascribed to OH^- groups resulting from deformation vibrations in HA [8,20,73,74]. The broad band around 3440–3570 cm^{-1} could be attributed to the water molecules adsorbed in the surface of FeCaP powders during samples' preparation [20,71,75,76].

According to the literature [8,10,20], the noticeable peaks at 1383 cm^{-1}, 1421 cm^{-1} and 1453 cm^{-1} could be assigned to the vibrational mode of carbonate (CO_3^{2-}) ions adsorbed from the atmosphere. The appearance of these bands, especially at high calcination temperatures, suggests the potential substitution of phosphate ions with carbonate ions in the crystal lattice of HA. Moreover, the presence of peaks corresponding to the CO_3^{2-} vibrational modes at lower wavenumbers, *e.g.*, 673, 741, 873 cm^{-1}, indicates that the carbonate ions are substituting OH

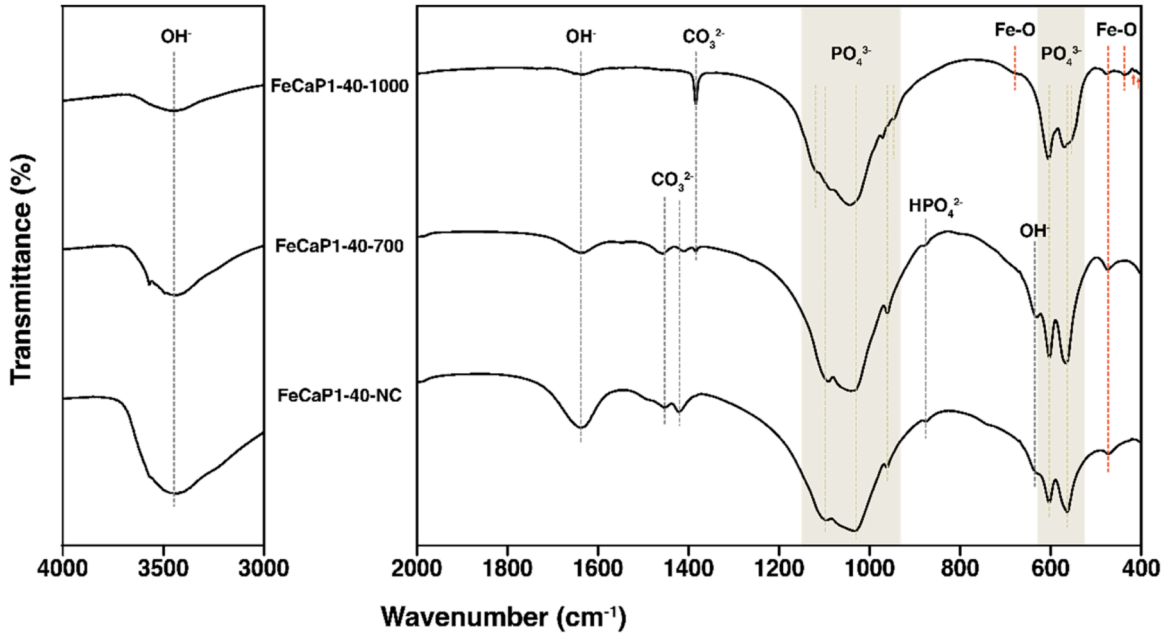

Fig. 3. FTIR spectra of FeCaP1–40 within the wavenumber range 4000–3000 cm^{-1} and 2000–400 cm^{-1} as a function of thermal treatment.

Table 4
FTIR assignments of functional groups of FeCaP1–40 powders as function of thermal treatment.

Assignments	Wavenumber (cm^{-1})			Ref.
	FeCaP1–40-NC	FeCaP1–40–700	FeCaP1–40–1000	
Fe-O	*	*	434	[61,76–79]
PO_4^{3-}	473 (ν_2); 565 (ν_4); 603 (ν_4); 960 (ν_1); 1033 (ν_3); 1095 (ν_3)	473 (ν_2); 568 (ν_4); 602 (ν_4); 962 (ν_1); 1039 (ν_3); 1091 (ν_3)	476 (ν_2); 567 (ν_4); 605 (ν_4); 1045 (ν_3); 1088 (ν_3); 1120 (ν_3)	[8,10,20,57,69–73,80]
OH^-	635 (ν_L); 1640 (ν_2); 3570 (ν_S)	631 (ν_L); 1640 (ν_2); 3570 (ν_S)	1640 (ν_2); 3449 (ν_S)	[8,10,20,57,69,71,73,76,80]
HPO_4^{2-}	873	878	-	[57]
CO_3^{2-}	673 (ν_4); 741 (ν_4); 873 (ν_2); 1383; 1421 (ν_3); 1453 (ν_3)	673 (ν_4); 878 (ν_2); 1383; 1410 (ν_3); 1458 (ν_3); 1546 (ν_3)	679 (ν_4); 1383	[20,70–72,74,80,81]

*no defined bands or peaks

groups within HA lattice (A-type HA) [70,81], contributing, together with the influence of iron incorporation, to the shifts in the lattice parameters determined by Rietveld analysis (Table 3). Consequently, the substitution of -OH group by CO_3^{2-} creates vacancies, thereby facilitating the introduction of Fe^{3+} into the apatite structure [68,69,82].

In the non-calcined and 700 °C calcined powders, a small peak around 873 cm^{-1} is visible, with its intensity noticeably less pronounced in the latter. This can be ascribed to HPO_4^{2-} group, indicative of the existence of calcium-deficient apatite phases [57]. The increase in the calcination temperature resulted also in a decrease in the vibrational modes of the OH groups, confirming a decrease in HA phases. These observations are all similar for the powders synthesised at 90 °C as can be seen in **Figure S2** in Supplementary Information.

The presence of iron oxide phases, like Fe_3O_4, is confirmed by the Fe-O vibrations that can be identified by the IR bands between 600 cm^{-1} and 360 cm^{-1}. For the FeCaP1–40 powder, as the thermal treatment temperature increases, the PO_4^{3-} band becomes broader with a small peak around 570 cm^{-1}, corresponding to the Fe-O stretching mode of tetrahedral and octahedral sites of the magnetite phase [77,83,84], as seen in the zoomed region in Fig. 4.

Moreover, maghemite phase can be identified in the same region, with two characteristic bands at 630 cm^{-1} and 430 cm^{-1} [8,61,77–79,84]. In fact, the possibility of having a coexistence of magnetite and maghemite as secondary phases [85] increases with the calcination temperature, as aforementioned. According to S. Nasrazadani et al. [77], magnetite tends to get quickly oxidized to a defective spinel close to maghemite at high temperatures. For the powders with a planned doubled iron molar concentration (FeCaP2–40–1000 and RefFeCaP-1000), the most intense peak of maghemite is shown as a small shoulder at 630 cm^{-1}, leading to a strong indication of the presence of this phase in both powders. Additionally, small bands can be detected around 430 cm^{-1} for all FeCaP powders, which leads us to believe that either maghemite or a defective spinel structure of magnetite is also formed [77]. In addition, a small shoulder around ~667 cm^{-1} is observed only in FeCaP1–1000 powders, suggesting a coordination effect of Fe^{3+} with PO_4^{3-}, according to Singh et al. [33]. These FTIR results thus appear to indicative the coexistence of Fe_3O_4 and γ-Fe_2O_3, since it is not possible to clearly differentiate these iron oxides from each other by XRD due to their very similar crystal structures.

Fig. 5 depicts the TG and DSC results of the FeCaP1–40, FeCaP1–90 and FeCaP2–40 powders, supporting the influence of the synthesis temperature and Fe molar concentration on the thermal behaviour of calcium phosphates. Consistent with the literature [86,87], synthesis conditions, including the method itself, reagents, temperature, pH and rinsing, significantly affect the thermal behaviour of HA/CaPs during heat treatment.

The TG results (Fig. 5a) show a continuous mass loss upon heating to 1000 °C for all FeCaP powders, with the most significant loss occurring between 24 and 400 °C. This mass loss is attributed to the release of thermally labile species such as water and hydrogen phosphate (HPO_4), as reported in prior studies [86–88]. Since the powders were synthesized via wet chemical precipitation using $FeCl_2{\cdot}4H_2O$ and $FeCl_3{\cdot}6H_2O$ as

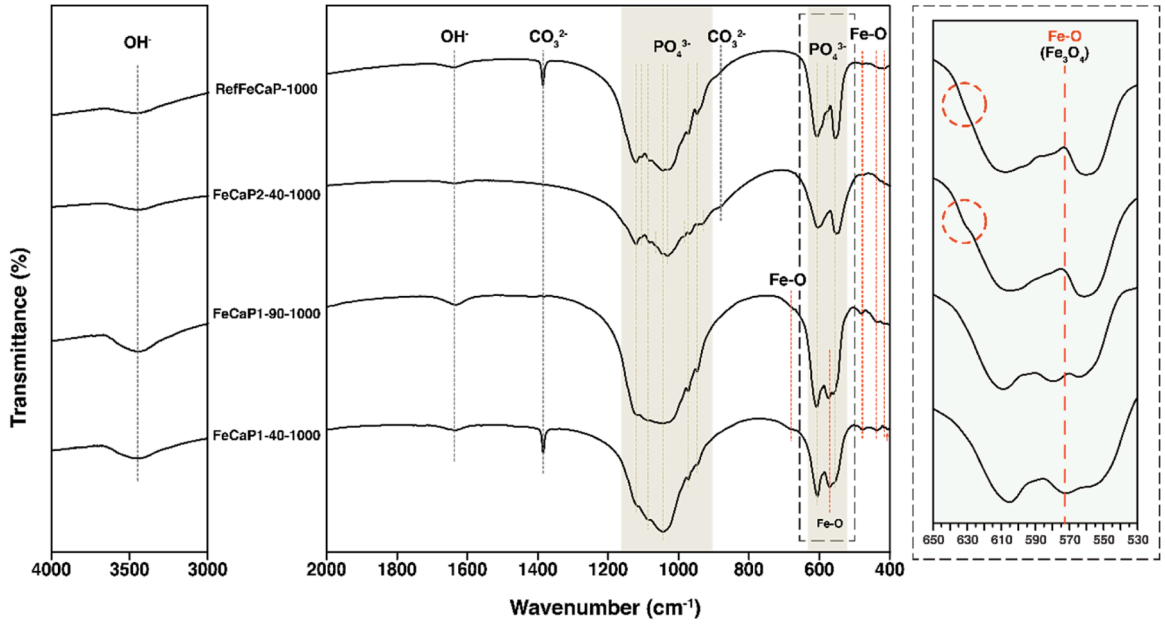

Fig. 4. FTIR spectra of FeCaP powders calcined at 1000 °C within the wavenumber range 4000–3000 cm^{-1}, 2000–400 cm^{-1} and zoomed region between 650–530 cm^{-1}. Red circles emphasize small shoulders in the region of the most intense IR maghemite peak [8,77–79,84].

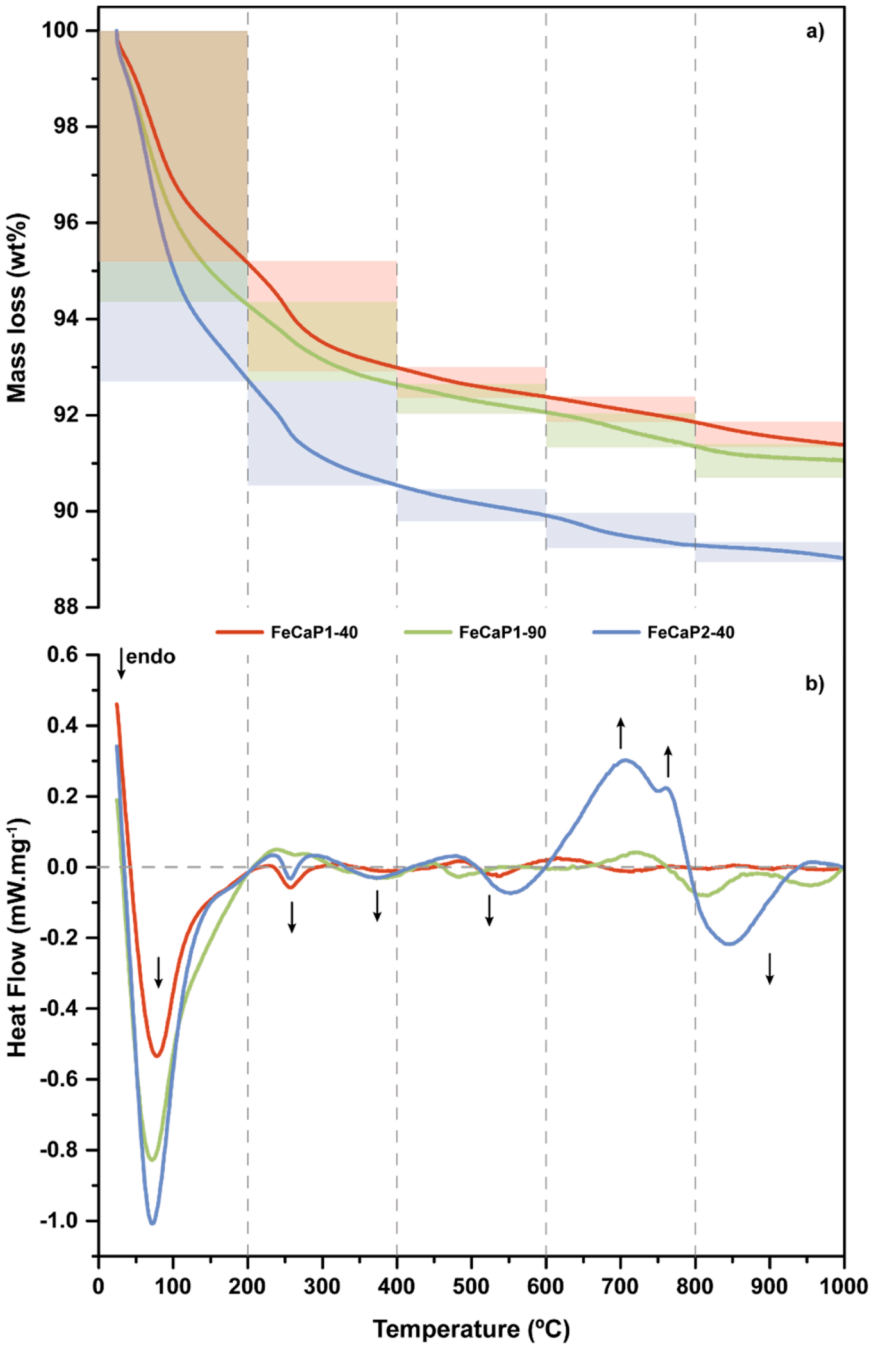

Fig. 5. (a) TG and (b) DSC curves for the FeCaP1–40, FeCaP1–90 and FeCaP2–40 powders under a heating rate of 5 K.min^{-1} in an inert Argon atmosphere.

Fe^{2+} and Fe^{3+} sources and subsequently rinsed, the incorporation of water into their structure is somewhat expected [88,89]. Notably, FeCaP2–40 undergoes a higher weight loss of approximately 10.97 wt%, compared to 8.61 wt% for FeCaP1–40 and 8.95 wt% for FeCaP1–90. This pronounced weight loss could be related to a higher hydration state in FeCaP2–40, as the increased Fe content could promote water retention within the structure. Further insight is provided by the DTG curves (see **Supplementary Information S3**), which clarify the mass loss trends observed in the TG analysis.

The DSC analysis (Fig. 5b) complements the TG results by elucidating the thermal phenomena associated with weight changes. For all FeCaP powders, two distinct areas with endothermic processes are observed up to ~400 °C. The first, occurring around 70–80 °C and 200–300 °C, can be attributed to the evaporation of physiosorbed water molecules. The second, between 300 and 400 °C, corresponds to the release of chemisorbed or lattice-bound water. These processes align with the mass loss trends observed in the TG analysis. Similarly, the deeper endothermic peak observed for FeCaP2–40 compared to FeCaP1–40 underscores its higher hydration state and greater weight loss.

In the 400–700 °C range, several endothermic events can be observed for all powders, some of them occurring at different temperatures for each powder. Previous studies [86–89] in synthetic apatites attribute the weight loss and the endothermic events in this temperature range to the condensation of HPO_4^{2-} groups, detected in FeCaP1–40 and FeCaP1–90 powders by FTIR analysis (Fig. 3, Table 4 and **Figure S2**), forming pyrophosphate ($P_2O_7^{4-}$) and releasing water. This phenomenon is indicative of the presence of a Ca-deficient HA structure, likely resulting from Fe incorporation into the lattice. Thermal

dehydroxylation further stabilizes P–O–P surface groups. Above 700 °C, the lack of sufficient Ca ions within the HA structure induces a phase transformation to β-TCP, stabilizing the material as a biphasic composite [89]. This transition is evidenced by exothermic events between 700–800 °C for FeCaP1–90 and FeCaP2–40 powders for both 5 K min^{-1} and 10 K min^{-1} heating rates, and only in 10 K min^{-1} for FeCaP1–40 (see Supplementary Information S4). The higher β-TCP content calculated via Rietveld refinement (Fig. 2) for these powders is corroborated by the observed exothermic reactions, and specifically a mass increase for FeCaP2–40, in TG measurements conducted at a higher heating rate of 10 K min^{-1} (see **Supplementary Information S4**).

The thermal analysis results reveal that both synthesis temperature and the introduced Fe molar concentration significantly influence the thermal behaviour of FeCaP powders. For a fixed Fe molar concentration and different synthesis temperatures, 40 °C and 90 °C in FeCaP1–40 and FeCaP1–90, respectively, similar weight loss percentages (~8.61 wt% and ~8.95 wt%, respectively) and comparable DSC profiles were observed. However, FeCaP1–40 seems to be more stable with thermal events less pronounced in DSC. This suggests that higher synthesis temperatures do not drastically affect the thermal stability of the FeCaP. In contrast, FeCaP2–40, synthesised at 40 °C but with higher Fe molar concentration, shows a higher weight loss (~10.97 wt%) and more pronounced endothermic and exothermic processes in the DSC results, indicating greater water retention and structural hydration due to increased Fe content. These findings demonstrate that Fe molar concentration plays a dominant role in influencing structural hydration and subsequent thermal behaviour, with higher Fe levels promoting water incorporation into the powder structure and more decomposition of HA phase into a biphasic composite with β-TCP.

Complementary techniques as ^{57}Mössbauer spectroscopy, Raman spectroscopy, X-ray Photoelectron Spectroscopy (XPS), wet chemical analysis, TEM were successfully employed in literature for the identification of their iron oxides especially when samples with a single phase are involved (magnetite or maghemite) [49,51,75,82]. Although ^{57}Mössbauer spectroscopy can provide more reliable quantitative data, the distinction between non-stoichiometric magnetite and the magnetite-maghemite mixture has been considered difficult [90]. Therefore, the results obtained in this work were analysed with these considerations in mind, leaving open the nature of the iron oxide fraction (magnetite, non-stoichiometric magnetite, maghemite or magnetite-maghemite mixture) detected by XRD and FTIR spectroscopy.

3.2. The role of processing conditions in structural and morphological features of FeCaP powders

Specific surface area, pore size, pore volume and density variation in FeCaP1 powders synthesised at different temperatures (40 and 90 °C), non-calcined (NC) and calcined at 700 °C and 1000 °C, as well as the powders containing higher amounts of iron calcined at 1000 °C (FeCaP2-40–1000 and RefFeCaP-1000), are presented in Table 5.

As expected, specific surface area decreases as calcination temperature increases for both FeCaP1 powders synthesised at 40 °C and 90 °C. Similarly, the average pore size and pore volume decrease with a concomitant increase in density values. Comparing the FeCaP1–40–1000 with FeCaP1–90–1000, values in the same order of magnitude were attained for SSA, average pore size and pore volume, demonstrating that this difference in synthesis temperature is not expressively influencing the size of resultant particles, although it was slightly smaller in the powders synthesised at 40 °C. The SSA decreases when the Fe amount increases for powders synthesised and calcined at the same temperature (FeCaP1–40–1000 < RefFeCaP-1000 < FeCaP2–40–1000), although the pore volume has not undergone significant changes.

Fig. 6a shows the TEM images of FeCaP1–40 and FeCaP1–90, non-calcined (NC) and after calcination at 700 °C and 1000 °C, while Fig. 6b presents the TEM images of FeCaP2–40 and RefFeCaP, both calcined at 1000 °C.

Non-calcined samples (FeCaP1–40-NC and FeCaP1–90-NC) seem to present nanometric particles with a non-uniform elongated shape, more perceptible for FeCaP1–40-NC sample (Fig. 6a top-left corner). Calcination temperature confers to the particles a more pronounced spherical shape and an increase of interfacial bonding among particles, resulting in particle agglomerates with higher sizes, in good agreement with SSA values presented in Table 5. Particles' morphology is similar for powders containing higher amounts of iron (RefFeCaP-1000 and FeCaP2–40–1000) after the calcination at 1000 °C, presenting bigger and rounder particles when compared to FeCaP1–40–1000 powder.

Looking in higher detail at crystalline particles of FeCaP1–40–1000 (Fig. 7), it is possible to observe that magnetite nanocrystals with diameters approximately 2–3 nm are incorporated in the bigger FeCaP particles. The atomic interplanar distances of these nanocrystals can be estimated to be ~ 2.10 Å, which are associated with the (2 0 -2 4) Miller indices of the Fd-3 m Fe_3O_4 structure – whose diffracted peak is also observed in the XRD patterns (Fig. 2). These small particles are embedded in larger (100–200 nm) particles, whose atomic interplanar distances of 2.42 and 2.52 Å can be attributed to crystalline β-TCP, diffracted at 2 Theta angles of 37.17° and 35.59° with Miller indices of (1 3 4) and (2 1 10), respectively. Alternatively, these distances could correspond to HA phases with a diffraction angle of 35.47° and Miller indices of (3 0 1).

The SEM micrographs with the EDS mappings regarding the distribution of Ca, Fe, and P ions in the samples with 4.8 and 9.8 wt% Fe content are presented in Fig. 8. In both samples, a homogeneous distribution of Fe, Ca and P ions throughout the particles is observed. It can be also notice from the images that primary particle sizes slightly increase as iron content increases, in good agreement with the SSA previously presented (Table 5). Regarding Fe elemental mapping, although it is not clearly perceptible that iron ions are present in higher overall concentration for the sample with 9.8 wt%, the dots corresponding to the iron ions seems to be bigger, indicating higher localised element content.

3.3. Influence of processing conditions on the magnetic behaviour of FeCaP powders

The room-temperature isothermal magnetization *versus* magnetic

Table 5
Specific surface area (SSA), pore size, pore volume and density of FeCaP powders attained in different synthesis and calcination conditions, as well as, in the presence of different amounts of iron.

Sample code	SSA (m^2 g^{-1}) (± 0.5 %)	Pore size (Avg.) (Å)	Pore volume (cm^3 g^{-1})	Density (g cm^{-3}) (± 0.1 %)
FeCaP1–40-NC	119.05 ± 0.39	257.90	0.53	2.99
FeCaP1–40–700	36.24 ± 0.09	99.77	0.08	3.29
FeCaP1–40–1000	8.61 ± 0.02	65.60	0.01	3.38
FeCaP1–90-NC	110.82 ± 0.37	165.82	0.47	3.03
FeCaP1–90–1000	7.29 ± 0.04	56.00	0.01	3.34
FeCaP2–40–1000	1.97 ± 0.01	61.23	0.003	3.33
RefFeCaP-1000	3.55 ± 0.01	56.77	0.01	3.55

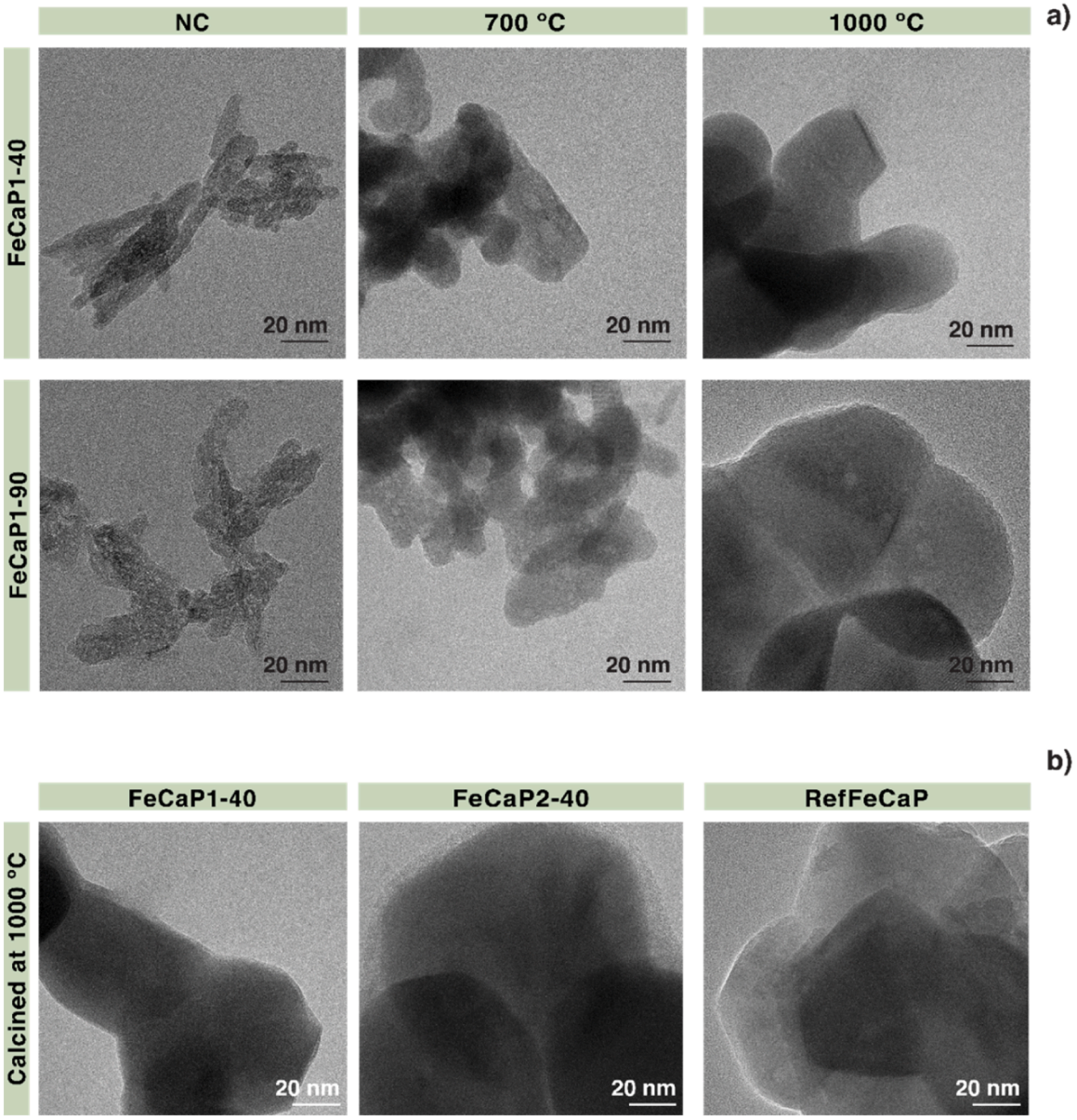

Fig. 6. TEM micrographs: (a) FeCaP1 powders synthesised at 40 and 90 °C, showing the influence of thermal treatment. (b) influence of Fe molar concentration in FeCaP-40 and RefFeCaP powders calcined at 1000 °C.

field curves of FeCaP powders calcined at 1000 °C are presented in Fig. 9. The total magnetic susceptibility (χ_{powder}) of a material or composite is the sum of the magnetic susceptibilities (χ_{powder}) of the different elements or structures present in the material or composite (Eq. 2). In the case of these powders, two major contributions are expected: 1) a ferro (χ_{ferro}) or superparamagnetic behaviour ($\chi_{superpara}$) of magnetite particles, which is dependent on their size; 2) a paramagnetic component (χ_{para}) of the iron ions that are located as a substitution ion in HA or β-TCP crystalline lattices.

$$\chi_{powder} = \chi_{ferro} + \chi_{superpara} + \chi_{para} \quad (2)$$

Overall, the magnetization curves display a predominant of a ferromagnetic contribution, as evidenced by the clear magnetic hysteresis and magnetization reaching a saturation at magnetic fields above 10 kOe. Additionally, a small paramagnetic contribution is also observable in all curves, characterized by a constant M(H) linear slope across the entire magnetic field range studied.

Two trends are worth highlighting for FeCaP1–40 powders (Fig. 9a) as the annealing temperature increases, (i) the saturation magnetization increases; (ii) the coercive field (H_c), remanent magnetization (M_{rem}) and consequently the hysteretic area increase. Remarkably, the non-calcined FeCaP1 (FeCaP1–40-NC) shows a superparamagnetic-like behaviour, with nearly null hysteresis.

For all FeCaP series subjected to calcination at 1000 °C (Fig. 9b), consistent trends are observed. The saturation magnetization increases proportionally with both the synthesis temperature (evidenced by the slightly higher Ms value of FeCaP1–90–1000 compared to FeCaP1-40–1000) and the Fe molar concentration (as indicated by M_s value: FeCaP1-40-1000 < RefFeCaP-1000 < FeCaP2–40–1000). Regarding the coercive field and remanent magnetization, FeCaP2–40–1000 powder exhibits trends similar to FeCaP1-40–1000. However, the reference powder (RefFeCaP-1000) shows a notably larger hysteretic area, along with elevated coercive field, and remanent magnetization values.

These two monotonous trends can be attributed to the increased presence of a ferromagnetic component in these samples, such as ferromagnetic magnetite. Annealing thermal treatments induce the sintering and growth of nanoparticles, resulting in the formation of

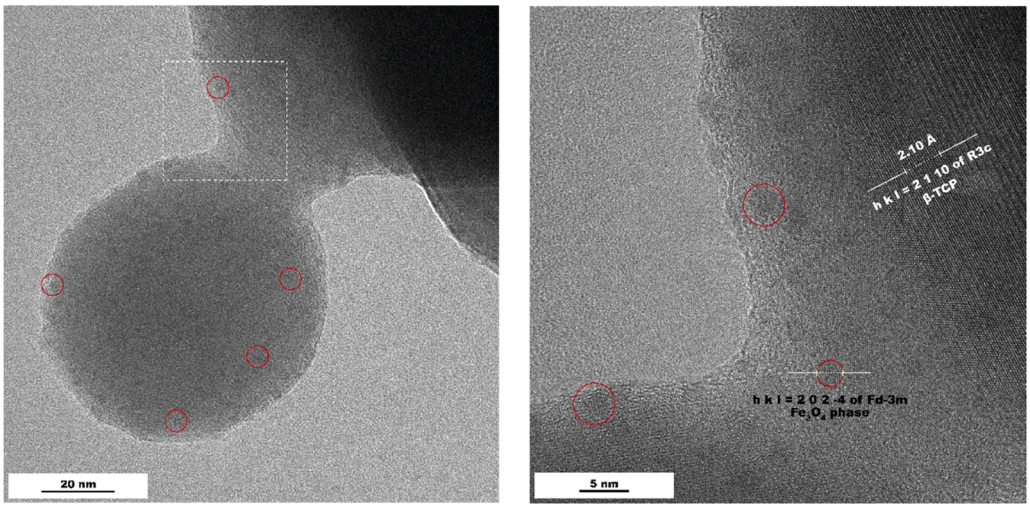

Fig. 7. TEM micrograph of FeCaP1–40–1000 powder. The red dots indicate the presence of small Fe_3O4 nanoparticles, verified by the interplanar distance of 2.10 Å, corresponding to hkl plane 2 0 2 -4. White arrows indicate a well-defined crystalline region of β-TCP, verified by the interplanar distance of 2.52 Å, corresponding to hkl plane 2 1 10.

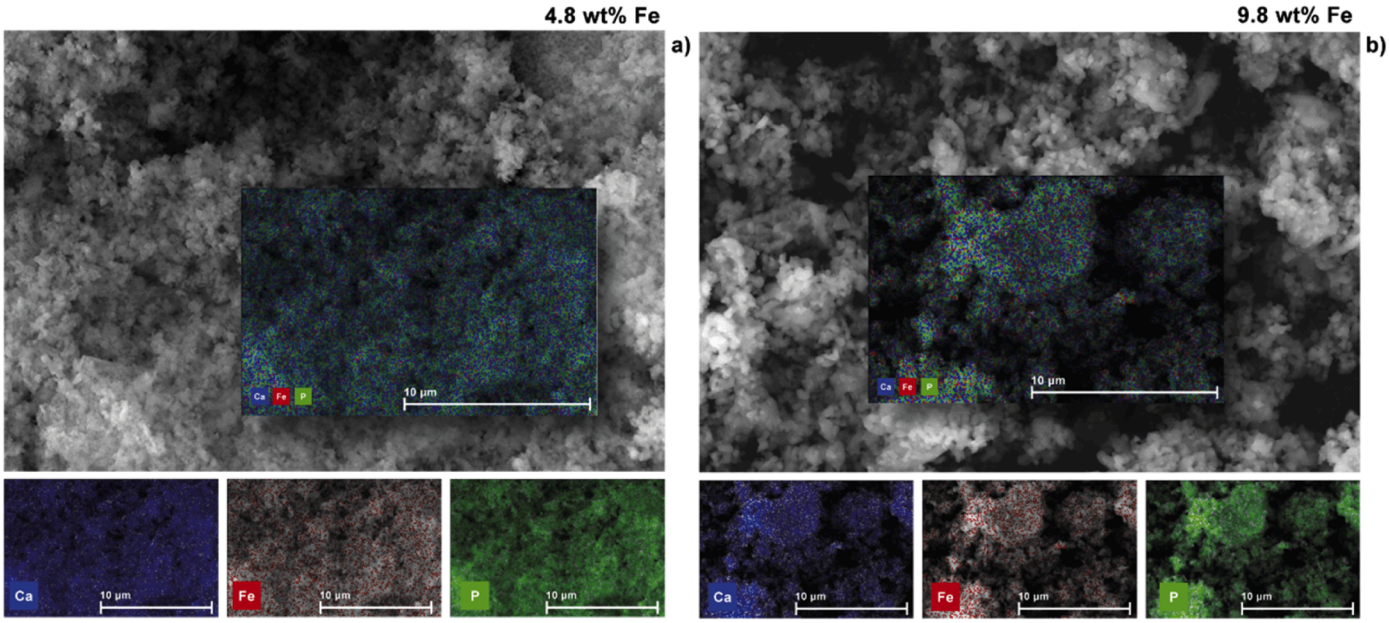

Fig. 8. SEM micrographs of the samples with EDS elemental mapping showing the distribution of Ca (blue), Fe (red) and P (green), in a magnification of x5K, for the samples with (a) 4.8 wt% and (b) 9.8 wt% of iron content.

larger multidomain and ferromagnetic magnetite nanostructures. Additionally, the increase in H_c, M_{rem} (and hysteretic area) with increasing calcination temperature (for both synthesis temperatures of 40 and 90 °C) also suggests that the amount of magnetite particles might be increasing, in accordance with theoretical models [91] and experimental studies [33,91–93] and further confirming the phase composition analysis derived from the Rietveld analysis (Fig. 2a-f).

3.4. *Thermo-responsiveness of FeCaP powders: magnetically induced heating*

Fig. 10 presents the temperature increase (ΔT) as a function of exposure time to alternating magnetic field (268 kHz and 200 Oe) for the FeCaP powders. The effects evaluated are: (i) calcination temperature while maintaining the synthesis temperature (Fig. 10a) and (ii) synthesis temperature (40 and 90 °C) and total Fe content (4.8 wt% and 9.8 wt%) for the powders calcined at the same temperature (1000 °C) (Fig. 10b). SAR evolution (normalised to Fe mass) *versus* β-TCP content in FeCaP powders calcined at 1000 °C is shown in Fig. 10c, to help clarify the trend observed on the magnetically induced heating curves (Fig. 10b).

According to the hyperthermia curves from Fig. 10a, FeCaP1–40-NC is the powder whose temperature increased the least, exhibiting a ΔT (t = 5min) ~3.5 °C. Higher temperatures were achieved for calcined samples, consistent with the enhanced ferromagnetic behaviour observed in Fig. 10a. However, a surprising behaviour was noted in the magnetically induced heating curves for FeCaP1–40 calcined at 700 °C and 1000 °C. FeCaP1–40–1000 exhibits a smaller temperature increase (~5 °C in 5 min) than the FeCaP1–40–700 (~7 °C in 5 min), despite the higher saturation magnetization of FeCaP1–40–1000. Similarly, when evaluating the impact of the synthesis temperature for FeCaP1 (Fig. 10b) on the hyperthermia capacity of the powders, it can be seen that increasing the synthesis temperature from 40 to 90 °C in the samples

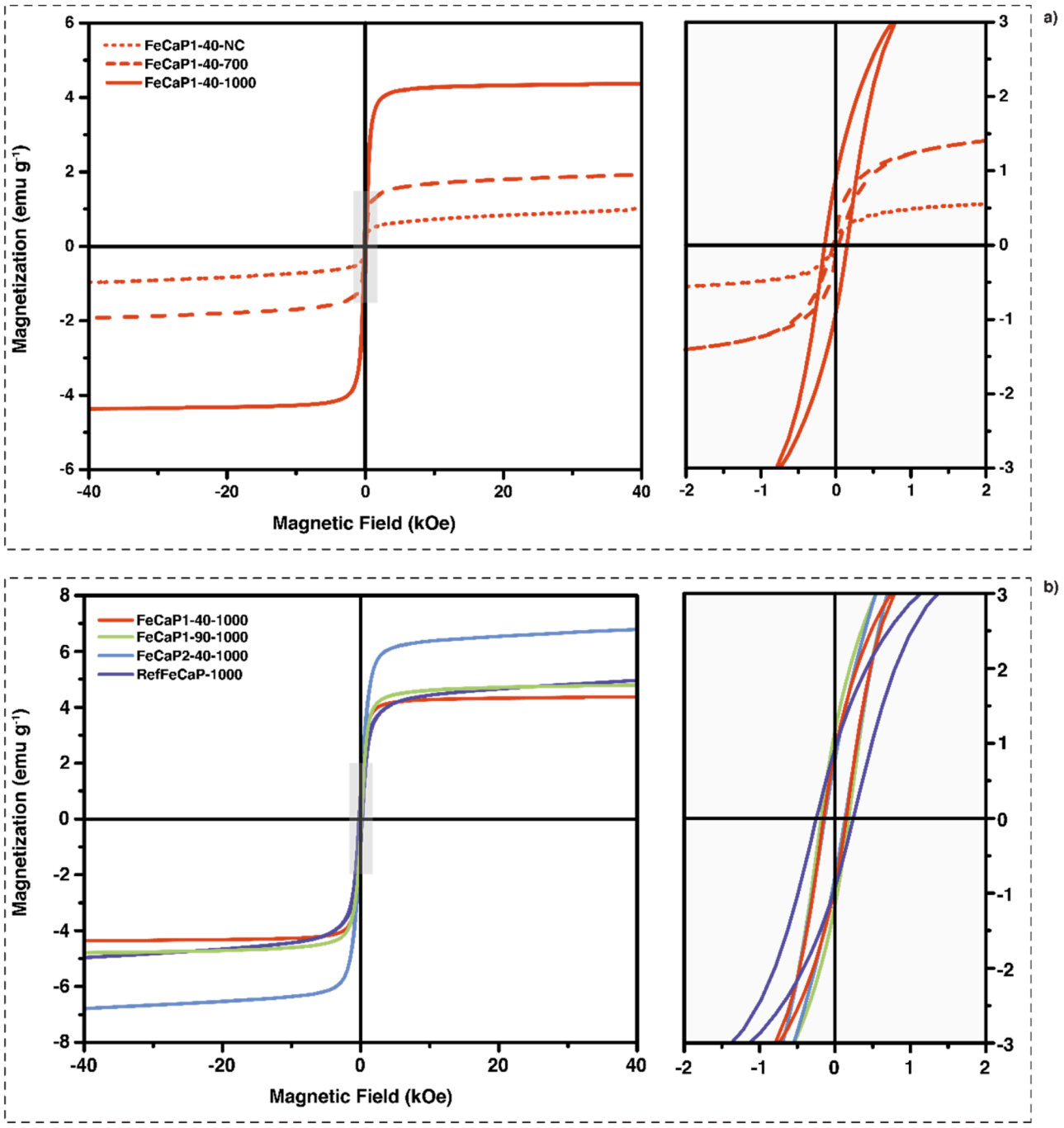

Fig. 9. Isothermal magnetization *versus* magnetic field curves measured at room temperature of (a) FeCaP1–40 powders heat-treated at different temperatures (NC, 700, 1000 °C) zoomed in an applied field interval of [-2,2] kOe and (b) FeCaP1 powders calcined 1000 °C, including powders with double amount of iron calcined at the same temperature (FeCaP2–10–1000 and RefFeCaP-1000) zoomed in an applied field interval of [-2,2] kOe.

calcined at 1000 °C, leads to a decrease in ΔT, although the saturation magnetization followed an opposite trend (Fig. 10b). Increasing the total Fe content from FeCaP1–40–1000 to FeCaP2–40–1000 also results in lower ΔT (Fig. 10b), while the saturation magnetization again presents an opposite trend (Fig. 9b).

SAR quantifies the rate at which electromagnetic energy is absorbed by a material and converted into heat within a given volume or mass and generally, higher SAR values imply greater heat generation potential [94–100]. Heating curves at 554 kHz and 869 kHz, together with SAR values of the powders, regarding the different tested frequencies (268, 554, and 869 kHz), are presented in Supplementary Information (**Figure S5** and **Table S5**, respectively). For the estimation of this parameter, the water heating capacity was considered as the medium for the measurements. An overall linear increase in SAR values for all powders as frequency increases is observed, in line with previous studies [98,101]. This emphasizes the relation between the frequency of the applied AC magnetic field and the resulting heat generation, which is fundamental for hyperthermia treatment optimization [94,98, 100–102]. These results clearly exemplify the complex correlation between SAR and magnetic properties – in particular, the saturation magnetization. The different induction heating mechanisms in magnetic nanoparticles immersed in different media and how heat propagates within such media is still the object of many studies [94]. In particular, the fact that SAR performance does not necessarily evolve

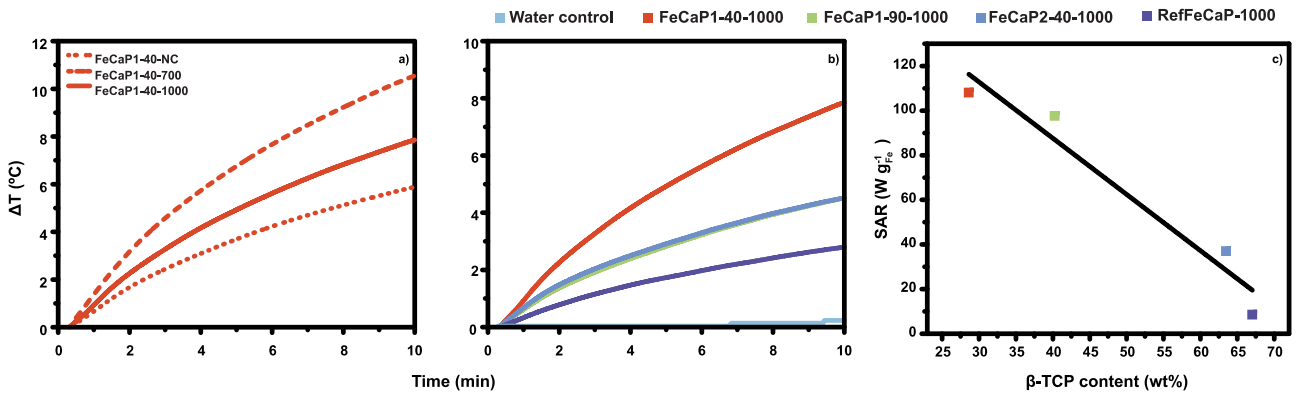

Fig. 10. Magnetic hyperthermia curves - Temperature increase as a function of exposure time to alternating magnetic field (268 kHz and 200 Oe) of (a) FeCaP1–40 non-calcined (NC) and calcined at different temperatures (700 and 1000 °C); (b) FeCaP powders synthesised at different synthesis temperatures (40 and 90 °C) and different total Fe content (4.8 wt% and 9.8 wt%) calcined at 1000 °C. The magnetic hyperthermia curve of a water control (straight line in light blue) is included for comparison purposes; (c) SAR (W g_{Fe}^{-1}) dependence on the β-TCP content (wt%) for FeCaP powders calcined at 1000 C.

monotonically with saturation magnetization, as reported in recent literature underscores the complex interplay of these phenomena [95].

This intriguing decoupling between saturation magnetization and magnetic hyperthermia properties can be hypothesized to originate from the complex phase composition resulting from the various synthesis and calcination conditions. In general, increasing the calcination temperature, synthesis temperature and Fe content in the FeCaP powders leads to an increase in the relative amount of magnetite in the samples. However, this increase in the amount of magnetite is accompanied in all the cases by a significant relative increase of the β-TCP phase. Despite the higher amount of magnetite in the samples, which perfectly correlates with an increasing saturation magnetization, the remarkable growth of the β-TCP phase could be responsible for a lower-than-expected magnetic heating efficiency. On the one hand, magnetic nanoparticles are embedded to a certain extent into the β-TCP matrix, limiting their heat transfer through the material to the solution. On the other hand, the thermal properties of this phase could make the heating capacity of magnetite nanoparticles more inefficient. Similar to the effect of the increasing calcination temperature, the phase composition analysis of the samples revealed that the increase of the synthesis temperature from 40 to 90 °C in the samples calcined at 1000 °C induced an increase of ~12 % of the crystalline β-TCP phase **(Table S6** in **Supplementary Information S6)**. Additionally, there is an increase in the amorphous phase as the synthesis temperature and the Fe content of the samples increase, moving from FeCaP1–40–1000 to FeCaP1–90–1000, and from FeCaP1–40–1000 to FeCaP2–40–1000, respectively (Fig. 2f and **Table S6**). This increase in the amorphous phase could also play a role in the heating performance of the powders. The presence of elevated β-TCP and amorphous phases can reduce heat transfer efficiency because of their relatively low thermal conductivity compared to metals and certain ceramics. Their electrical insulating properties and porous structures hinder thermal conductivity, significantly impacting material's heat dissipation performance. Further analysis including thermal diffusion and conductivity, along with numerical simulations, would help elucidate the impact of the β-TCP phase on the overall heating properties of FeCaP powders. The effects of specific surface area and particle size and morphology on the magnetic heating efficiency of the FeCaP powders, as well as the presence of intrinsic Fe phases in the CaP lattice, cannot be disregarded. Furthermore, it is particularly important to emphasise that the isothermal magnetization *versus* applied field curves presented in Fig. 9 were obtained by DC (static fields) measurements in contrast with the intrinsically dynamic nature of the hyperthermia measurements (AC fields with frequencies ranging up to 869 kHz and amplitudes of 200 Oe; see **Figure S5** in Supplementary Information). This distinction is particularly relevant as, for nearly all measured samples a -200 to +200 Oe field cycle falls well within the measured DC hysteretic area (Fig. 9).

A linear-like decrease of SAR is observed with increasing β-TCP content (w%) for the FeCaP powders calcined at 1000 °C (Fig. 10c). Notably, FeCaP1–40–1000 exhibits the highest SAR and heating capacity, even when compared to the RefFeCaP-1000 and FeCaP2–40–1000 powders, which contain almost double the total iron content (Table 2). These results, combined with the fact that the magnetite content in FeCaP1–40–1000 does not significantly differ from that of RefFeCaP-1000 and FeCaP2–40–1000 (Table 2), suggest the presence of other species besides magnetite that contribute to the total iron amount but weaken the magnetically induced heating. Moreover, these Fe-based phases coexist with the increase of the β-TCP amount in both FeCaP2-40–1000 and RefFeCaP-1000 samples, which hinders heat transfer through the material compared to FeCaP1–40–1000. Furthermore, although the Fe content measured by ICP is the same for RefFeCaP-1000 and FeCaP2–40–1000 powders (9.8 wt%), the magnetite content quantified by the Rietveld method differs by 1 wt% (Table 2). This difference could account for the lower SAR and hyperthermia performance observed for the RefFeCaP-1000 powder.

These results highlight the complexity of the phase composition – property relationship in FeCaP powders. This study underscores the importance of carefully optimizing synthesis and calcination parameters to achieve desired magnetic properties and effective hyperthermia performance, contributing valuable insights for future applications in magnetic materials and the biomedical field.

Furthermore, for a better comprehension of the work here discussed, the synthesis conditions and the resulting properties of the studied FeCaP powders are summarised in a table format in Supplementary Information S6. This table reflects how small variations in synthesis conditions, as the synthesis temperature, pH or the Fe content can affect the final properties of the powders, providing a clear overview of the trends observed in this study.

4. Conclusions

This study elucidates the intricate interplay between synthesis conditions, phase composition, and particle characteristics in determining the magnetic and hyperthermia performance of CaP-based powders. Significant advancements have been demonstrated in the synthesis and characterization of highly crystalline magnetic CaP-based powders through calcination at 1000 °C.

The synthesis of FeCaP1 at 40 °C and further calcination at 1000 °C results in CaP particles with magnetite phase distributed and embedded within the CaP matrix. These distinctive structural characteristics play a key role in the material's behaviour under oxidative conditions. When exposed to an oxidizing atmosphere at 600 °C, no significant transformation to hematite is observed. The absence of this transformation suggests that the magnetite embedded within the CaP matrix remains

stable under these conditions, maintaining its structure. This behaviour contrasts with that of the other powders, particularly in those with higher iron concentrations (FeCaP2 and RefFeCaP), where the transformation to hematite is more noticeable.

The enhanced stability of magnetite in FeCaP1–40–1000 can be attributed to the distribution and embedding of magnetite within the CaP matrix, which likely protects it from oxidation and transformation into hematite. Furthermore, the smaller particle size and the higher presence of hydroxyapatite in FeCaP1–40–1000 contribute to the stability of the magnetite phase during heat treatment. This stability makes FeCaP1–40–1000 a promising candidate for applications, where maintaining the magnetic phase stable under high-temperature or oxidative conditions is essential.

For biomedical applications, such as drug delivery or hyperthermia treatments, the stability of magnetite in FeCaP1–40–1000 is particularly relevant. Although biological environment conditions at 37 °C are much less extreme when compared to those at 600 °C, the magnetite embedded within the CaP matrix may provide protection from immediate oxidation into hematite, reducing the direct exposure of magnetite to oxidative agents, such as oxygen in body fluids. This structural protection may extend the magneto-thermal properties of magnetite, further enhancing the potential use of FeCaP1–40–1000 powder in the biomedical field, including bone regeneration and local magnetic hyperthermia therapy.

Moreover, CaP materials are widely recognized for their potential in bone regeneration, and incorporating iron ions could further enhance their bioactivity, as iron plays essential roles in enzymatic processes, oxygen transport, and collagen synthesis. Given the influence of magnetic fields on these processes, the development of intrinsically magnetic calcium phosphate materials—without requiring the addition of magnetic nanoparticles—emerges as a promising path for multifunctional magnetic bone substitutes. Therefore, these findings highlight the necessity of carefully optimizing synthesis and calcination parameters to achieve the desired magneto-thermal properties. The insights gained from this study provide valuable knowledge for the fabrication of magnetic components with future potential applications in the biomedical field, including bone regeneration and local magnetic hyperthermia therapy.

CRediT authorship contribution statement

Tânia S.S. Carvalho: Writing – original draft, Methodology, Investigation, Formal analysis, Data curation, Conceptualization. **João H. Belo:** Writing – review & editing, Validation, Supervision, Methodology, Investigation, Formal analysis, Data curation. **João C.C. Abrantes:** Writing – review & editing, Validation, Resources, Methodology, Formal analysis, Data curation. **Manuel Bañobre-López:** Writing – review & editing, Validation, Resources, Methodology, Formal analysis, Data curation. **Diogo Lopes:** Writing – original draft, Methodology. **Andrei V. Kovalevsky:** Writing – review & editing, Validation, Resources. **A. Kaushal:** Methodology. **João P. Araújo:** Writing – review & editing, Validation, Resources. **Susana M. Olhero:** Writing – review & editing, Validation, Supervision, Resources, Investigation, Funding acquisition, Formal analysis, Conceptualization. **Paula M.C. Torres:** Writing – review & editing, Validation, Supervision, Resources, Investigation, Funding acquisition, Formal analysis, Conceptualization.

Declaration of competing interest

The authors declare that they have no known competing financial interests or personal relationships that could have appeared to influence the work reported in this paper.

Acknowledgements

T. S. S. Carvalho wishes to thank Fundação para a Ciência e Tecnologia (FCT) for supporting their work with a PhD grant (https://doi.org/10.54499/2021.06481.BD). This study was funded by European Union's Horizon 2020 research and innovation programme under the scope of InterLynk project with grant agreement no. 953169.

This work is also funded by FEDER funds through the COMPETE 2020 Programme and National Funds through FCT- Portuguese Foundation for Science and Technology under the projects 2BBone and FlexMicroDerm with references POCI-01–0145-FEDER-029940 (PTDC/CTM-CER/29940/2017) and POCI-01–0145-FEDER-029274 (PTDC/BTM-MAT/29274/2017), respectively. The authors also acknowledge the project CICECO-Aveiro Institute of Materials, UIDB/50011/2020 (DOI 10.54499/UIDB/50011/2020), UIDP/50011/2020 (DOI 10.54499/UIDP/50011/2020) & LA/P/0006/2020 (DOI 10.54499/LA/P/0006/2020), financed by national funds through the FCT/MCTES (PIDDAC) and when appropriate co-financed by FEDER under the PT2020 Partnership Agreement. J. H. Belo would like to acknowledge projects PTDC/EMETED/3099/2020, UIDP/04968/2020-Programático, UIDB/04968/2020, NECL-NORTE-010145-FEDER022096 and CERN/FISTEC/0003/2019; and FCT for his contract DL57/2016 reference SFRH-BPD-87430/2012. Diogo Lopes acknowledges the PhD scholarship by FCT (grant https://doi.org/10.54499/2020.06454.BD) and P. M. C. Torres acknowledge FCT for 2023.07934.CEECIND. Part of this work was also carried out in part through the use of the INL User Facilities.

Supplementary materials

Supplementary material associated with this article can be found, in the online version, at doi:10.1016/j.materresbull.2024.113274.

Data availability

Data will be made available on request.

References

[1] Y. Xia, H. Chen, Y. Zhao, F. Zhang, X. Li, L. Wang, M.D. Weir, J. Ma, M. A. Reynolds, N. Gu, H.H.K. Xu, Novel magnetic calcium phosphate-stem cell construct with magnetic field enhances osteogenic differentiation and bone tissue engineering, Mater. Sci. and Eng. C 98 (2019) 30–41, https://doi.org/10.1016/j.msec.2018.12.120.

[2] Ashokan K.M. Sajesh, G.S. Gowd, T.B. Sivanarayanan, A.K.K. Unni, S.V. Nair, M. Koyakutty, Magnetic 3D scaffold: A theranostic tool for tissue regeneration and non-invasive imaging *in vivo*, Nanomedicine 18 (2019) 179–188, https://doi.org/10.1016/j.nano.2019.02.022.

[3] S. Singh, G. Singh, N. Bala, Synthesis and characterization of iron oxide-hydroxyapatite-chitosan composite coating and its biological assessment for biomedical applications, Prog. Org. Coat. 150 (2021) 106011, https://doi.org/10.1016/j.porgcoat.2020.106011.

[4] A.F.M. Rodrigues, P.M.C. Torres, M.J.S. Barros, R. Presa, N. Ribeiro, J.C. C. Abrantes, J.H. Belo, J.S. Amaral, V.S. Amaral, M. Bañobre-López, A. Bettencourt, A. Sousa, S.M. Olhero, Effective production of multifunctional magnetic-sensitive biomaterial by an extrusion-based additive manufacturing technique, Biomedical Mater. 16 (2021) 015011, https://doi.org/10.1088/1748-605X/abac4c.

[5] T.S.S. Carvalho, P.M.C. Torres, J.H. Belo, J. Mano, S.M. Olhero, Bioactive magnetic materials in bone tissue engineering: a review of recent findings in CaPBased particles and 3D-printed scaffolds, Adv. Nanobiomed Res. 3 (2023) 2300035, https://doi.org/10.1002/anbr.202300035.

[6] Y. Xu, F. Zhang, W. Zhai, S. Cheng, J. Li, Y. Wang, Unraveling of Advances in 3D-Printed Polymer-Based Bone Scaffolds, Polymers 14 (2022) 566, https://doi.org/10.3390/polym14030566.

[7] T.S.S. Carvalho, N. Ribeiro, P.M.C. Torres, J.C. Almeida, J.H. Belo, J.P Araújo, A. Ramos, M. Oliveira, S.M Olhero, Magnetic polylactic acid-calcium phosphate-based biocomposite as a potential biomaterial for tissue engineering applications, Mater. Chem. Phys. 296 (2023) 127175, https://doi.org/10.1016/j.matchemphys.2022.127175.

[8] A. Biedrzycka, E. Skwarek, U.M. Hanna, Hydroxyapatite with magnetic core: synthesis methods, properties, adsorption and medical applications, Adv. Colloid Interf. Sci. 291 (2021) 102401, https://doi.org/10.1016/j.cis.2021.102401.

[9] A. Mushtaq, R. Zhao, D. Luo, E. Dempsey, X. Wang, M.Z. Iqbal, X. Kong, Magnetic hydroxyapatite nanocomposites: the advances from synthesis to biomedical applications, Mater. Des. 197 (2021) 109269, https://doi.org/10.1016/j.matdes.2020.109269.

[10] S.C. Veerla, D.R. Kim, J. Kim, H. Sohn, S.Y. Yang, Controlled nanoparticle synthesis of Ag/Fe co-doped hydroxyapatite system for cancer cell treatment,

Mater. Sci. and Eng. C 98 (2019) 311–323, https://doi.org/10.1016/j.msec.2018.12.148.
[11] A. Karthika, Biocompatible iron and copper incorporated nanohydroxyapatite coating for biomedical implant applications, Mater. Today Proc 51 (2012) 1754–1759, https://doi.org/10.1016/j.matpr.2020.12.813.
[12] K. Sangeetha, G. Vidhya, E.K. Girija, M. Ashok, Fabrications of magnetic responsive hydroxyapatite platform: *in vitro* release of chemo drug for cancer therapy, Mater. Today Proc 26 (2019) 3579–3582, https://doi.org/10.1016/j.matpr.2019.08.153.
[13] F. Zhuang, R. Tan, W. Shen, X. Zhang, W. Xu, W. Song, Monodisperse magnetic hydroxyapatite/Fe_3O_4 microspheres for removal of lead(II) from aqueous solution, J. Alloys Compd. 637 (2015) 531–537, https://doi.org/10.1016/j.jallcom.2015.02.216.
[14] S. Periyasamy, V. Gopalakannan, N. Viswanathan, Hydrothermal assisted magnetic nano-hydroxyapatite encapsulated alginate beads for efficient Cr(VI) uptake from water, J. Environ. Chem. Eng. 6 (2018) 1443–1454, https://doi.org/10.1016/j.jece.2018.01.007.
[15] Q. Zhang, S. Dan, K. Du, Fabrication and characterization of magnetic hydroxyapatite entrapped agarose composite beads with high adsorption capacity for heavy metal removal, Ind. Eng. Chem. Res. 56 (2017) 8705–8712, https://doi.org/10.1021/acs.iecr.7b01635.
[16] J.A. Ramos-Guivar, M.A. Morales, F.J. Litterst, γ-Fe_2O_3 nanoparticles embedded in nanohydroxyapatite matrix for magnetic hyperthermia and *in vitro* osteoblast cell studies, Ceram. Int. 46 (2020) 10658–10666, https://doi.org/10.1016/j.ceramint.2020.01.072.
[17] A. Vahdat, B. Ghasemi, M. Yousefpour, Synthesis of hydroxyapatite and hydroxyapatite/Fe_3O_4 nanocomposite for removal of heavy metals, Environ. Nanotechnol. Monit. Manag. 12 (2019) 100233, https://doi.org/10.1016/j.enmm.2019.100233.
[18] L. Gu, X. He, Z. Wu, Mesoporous Fe_3O_4/hydroxyapatite composite for targeted drug delivery, Mater. Res. Bull. 59 (2014) 65–68, https://doi.org/10.1016/j.materresbull.2014.06.018.
[19] S. Murakami, T. Hosono, B. Jeyadevan, M. Kamitakahara, K. Ioku, Hydrothermal synthesis of magnetite/hydroxyapatite composite material for hyperthermia therapy for bone cancer, J. Cer. Soc. of Japan 116 (2008) 950–954, https://doi.org/10.2109/jcersj2.116.950.
[20] K.A. Al Jahoushi, A.I. Ayesh, H.F. El-Maghraby, W. Alnoush, D. Higgins, F. M. Hassan, Y.E. Greish, Tunable hydroxyapatite/magnetite nanohybrids with preserved magnetic properties, Adv. Mater. Interf. 9 (2022) 2102120, https://doi.org/10.1002/admi.202102120.
[21] T. Kobayashi, Cancer hyperthermia using nanomagnetic particles and induction of immune responses, in: V. Torchilin (Ed.), Handbook of Nanobiomedical Research, World Scientific Publishing, Singapore, 2014, pp. 465–499, https://doi.org/10.1142/9789814520652_0032.
[22] L.S. Arias, J.P. Pessan, A.P.M. Vieira, T.M.T. De Lima, A.C.B. Delbem, D. R. Monteiro, Iron oxide nanoparticles for biomedical applications: a perspective on synthesis, drugs, antimicrobial activity, and toxicity, Antibiotics 7 (2018) 46, https://doi.org/10.3390/antibiotics7020046.
[23] E.C. Abenojar, S. Wickramasinghe, J. Bas-Concepcion, A.C.S. Samia, Structural effects on the magnetic hyperthermia properties of iron oxide nanoparticles, Prog. in Nat. Sci.: Mater. Intern. 26 (2016) 440–448, https://doi.org/10.1016/j.pnsc.2016.09.004.
[24] G. Liu, J. Gao, H. Ai, X. Chen, Applications and potential toxicity of magnetic iron oxide nanoparticles, Small 9 (2013) 1533–1545, https://doi.org/10.1002/smll.201201531.
[25] N. Singh, G.J.S. Jenkins, R. Asadi, S.H. Doak, Potential toxicity of superparamagnetic iron oxide nanoparticles (SPION), Nano Rev 1 (2010) 5358, https://doi.org/10.3402/nano.v1i0.5358.
[26] Y. Wang, W. Zhai, H. Zhang, S. Cheng, J. Li, Injectable polyzwitterionic lubricant for complete prevention of cardiac adhesion, Macromol. Biosci. 23 (2023) 2200554, https://doi.org/10.1002/mabi.202200554.
[27] Y. Wang, W. Zhai, J. Li, H. Liu, C. Li, J. Li, Friction behavior of biodegradable electrospun polyester nanofibrous membranes, Tribol. Int. 188 (2023) 108891, https://doi.org/10.1016/j.triboint.2023.108891.
[28] C.L. Ying Kei, Iron-substituted hydroxyapatite, in: A.S. Khan, A.A. Chaudhry (Eds.), Handbook of Ionic Substituted Hydroxyapatites, Woodhead Publishing, United Kingdom, 2019, pp. 259–282, https://doi.org/10.1016/B978-0-08-102834-6.00011-2.
[29] S. Jose, M. Senthilkumar, K. Elayaraja, M. Haris, A. George, A.D. Raj, S. J. Sundaram, A.K.H. Bashir, M. Maaza, K. Kaviyarasu, Preparation and characterization of Fe-doped n-hydroxyapatite for biomedical application, Surf. and Interf. 25 (2021) 101185, https://doi.org/10.1016/j.surfin.2021.101185.
[30] A. Tampieri, T. D'Alessandro, M. Sprio, E. Landi, L. Bertinetti, S. Panseri, G. Pepponi, J. Goettlicher, M. Bañobre-López, J. Rivas, Intrinsic magnetism and hyperthermia in bioactive Fe-doped hydroxyapatite, Acta Biomater. 8 (2012) 843–851, https://doi.org/10.1016/j.actbio.2011.09.032.
[31] N.A. Mata, P. Ros-Tárraga, P. Velasquez, A. Murciano, P.N. De Aza, New iron-doped multilayer ceramic scaffold with noncontinuous bioactive behavior, Ceram. Int. 46 (2020) 16388–16396, https://doi.org/10.1016/j.ceramint.2020.03.198.
[32] F.P. Filho, R.E.F.Q. Nogueira, M.P.F. Graça, M.A. Valente, A.S.B. Sombra, C. C. Silva, Structural and mechanical study of the sintering effect in hydroxyapatite doped with iron oxide, Physica B Condens. Matter. 403 (2008) 3826–3829, https://doi.org/10.1016/j.physb.2008.07.017.
[33] R.K. Singh, M. Srivastava, N.K. Prasad, S. Awasthi, A. Dhayalan, S. Kannan, Iron doped β-tricalcium phosphate: synthesis, characterization, hyperthermia effect, biocompatibility and mechanical evaluation, Mater. Sci. and Eng. C 78 (2017) 715–726, https://doi.org/10.1016/j.msec.2017.04.130.
[34] M.E. Zilm, L. Yu, W.A. Hines, M. Wei, Magnetic properties and cytocompatibility of transition-metal-incorporated hydroxyapatite, Mater. Sci. and Eng. C 87 (2018) 112–119, https://doi.org/10.1016/j.msec.2018.02.018.
[35] V. Uskoković, V. Graziani, V.M. Wu, I.V. Fadeeva, A.S. Fomin, I.A. Presniakov, M. Fosca, M. Ortenzi, R. Caminiti, J.V. Rau, Gold is for the mistress, silver for the maid: Enhanced mechanical properties, osteoinduction and antibacterial activity due to iron doping of tricalcium phosphate bone cements, Mater. Sci. and Eng. C 94 (2019) 798–810, https://doi.org/10.1016/j.msec.2018.10.028.
[36] L. Sinusaite, A. Popov, A. Antuzevics, K. Mazeika, D. Baltrunas, J.C. Yang, J. L. Horng, S. Shi, T. Sekino, K. Ishikawa, A. Kareiva, A. Zarkov, Fe and Zn co-substituted beta-tricalcium phosphate (β-TCP): Synthesis, structural, magnetic, mechanical and biological properties, Mater. Sci. and Eng. C 112 (2020) 110918, https://doi.org/10.1016/j.msec.2020.110918.
[37] R. Panneerselvam, N. Anandhan, G. Gopu, A. Amali Roselin, K.P. Ganesan, T. Marimuthu, Impact of different transition metal ions in the structural, mechanical, optical, chemico-physical and biological properties of nanohydroxyapatite, Appl. Surf. Sci. 506 (2020) 144802, https://doi.org/10.1016/j.apsusc.2019.144802.
[38] E. Boanini, M. Gazzano, A. Bigi, Ionic substitutions in calcium phosphates synthesized at low temperature, Acta Biomater. 6 (2010) 1882–1894, https://doi.org/10.1016/j.actbio.2009.12.041.
[39] N. Abbaspour, R. Hurrell, R. Kelishadi, Review on iron and its importance for human health, J. Res. Med. Sci. 19 (2014) 164–174. http://www.ncbi.nlm.nih.gov/pmc/articles/pmc3999603/.
[40] C. Pucci, A. Degl'Innocenti, M. Belenli Gümüş, G. Ciofani, Superparamagnetic iron oxide nanoparticles for magnetic hyperthermia: recent advancements, molecular effects, and future directions in the omics era, Biomater. Sci. 10 (2022) 2103–2121, https://doi.org/10.1039/d1bm01963e.
[41] S. Laurent, S. Dutz, U.O. Häfeli, M. Mahmoudi, Magnetic fluid hyperthermia: Focus on superparamagnetic iron oxide nanoparticles, Adv.in Colloid and Interf. Sci. 166 (2011) 8–23, https://doi.org/10.1016/j.cis.2011.04.003.
[42] R.K. Singh, M. Srivastava, N.K. Prasad, P.H. Shetty, S. Kannan, Hyperthermia effect and antibacterial efficacy of Fe^{3+}/Co^{2+} co-substitutions in β-$Ca_3(PO_4)_2$ for bone cancer and defect therapy, J. Biomed. Mater. Res. B Appl. Biomater. 106 (2018) 1317–1328, https://doi.org/10.1002/jbm.b.33921.
[43] S. Balakrishnan, V.P. Padmanabhan, R. Kulandaivelu, T.S.S.N. Nellaiappan, S. Sagadevan, S. Paiman, F. Mohammad, H.A. Al-Lohedan, P.K. Obulapuram, W. C. Oh, Influence of iron doping towards the physicochemical and biological characteristics of hydroxyapatite, Ceram. Int. 47 (2021) 5061–5070, https://doi.org/10.1016/j.ceramint.2020.10.084.
[44] Z. Sheikh, M.-N. Abdallah, A. Hanafi, S. Misbahuddin, H. Rashid, M. Glogauer, Mechanisms of *in vivo* degradation and resorption of calcium phosphate based biomaterials, Materials 8 (2015) 7913–7925, https://doi.org/10.3390/ma8115430.
[45] A. Marnot, A. Dobbs, B. Brettmann, Material extrusion additive manufacturing of dense pastes consisting of macroscopic particles, MRS Comm. 12 (2022) 483–494, https://doi.org/10.1557/s43579-022-00209-1.
[46] A. Marnot, K. Koube, S. Jang, N. Thadhani, J. Kacher, B. Brettmann, Material extrusion additive manufacturing of high particle loaded suspensions: a review of materials, processes and challenges, Virtual and Phys. Prototyp. 18 (2023) e2279149, https://doi.org/10.1080/17452759.2023.2279149.
[47] I. Campbell, A. Marnot, M. Ketcham, C. Travis, B. Brettmann, Direct ink write 3D printing of high solids loading bimodal distributions of particles, AlChE J. 67 (2021) e17412, https://doi.org/10.1002/aic.17412.
[48] M. Mohammadi, G. Becker, S. Diener, J.M. Tulliani, N. Katsikis, P. Palmero, Robocasting of dense zirconia parts using commercial yttria-stabilized zirconia granules and ultrafine particles. Paste preparation, printing, mechanical properties, Ceram. Int. 48 (2022) 1936–1946, https://doi.org/10.1016/j.ceramint.2021.09.278.
[49] J. Winsett, A. Moilanen, K. Paudel, S. Kamali, K. Ding, W. Cribb, D. Seifu, S. Neupane, Quantitative determination of magnetite and maghemite in iron oxide nanoparticles using Mössbauer spectroscopy, SN Appl. Sci. 1 (2019) 1636, https://doi.org/10.1007/s42452-019-1699-2.
[50] M.R. Zachariah, M.I. Aquino, R.D. Shull, E.B. Steel, Formation of superparamagnetic nanocomposites from vapor phase condensation in a flame, Nanostruc. Mater. 5 (1995) 383–392, https://doi.org/10.1016/0965-9773(95)00260-L.
[51] T. Girardet, S. Diliberto, C. Carteret, F. Cleymand, S. Fleutot, Determination of the percentage of magnetite in iron oxide nanoparticles: a comparison between Mössbauer spectroscopy and Raman spectroscopy, Solid State Sci. 143 (2023) 107258, https://doi.org/10.1016/j.solidstatesciences.2023.107258.
[52] S. Raynaud, E. Champion, D. Bernache-Assollant, P. Thomas, Calcium phosphate apatites with variable Ca/P atomic ratio I. Synthesis, characterisation and thermal stability of powders, Biomater 23 (2002) 1065–1072, https://doi.org/10.1016/S01429612(01)002186.
[53] A. El Yacoubi, Proprietes Structurales D'Hydroxyapatites Silicatees Et Elaboration Des Systemes Composites A Base D'Orthophosphate D'Argent/Hydroxyapatite En Vue D'Applications Photocatalytiques Et Antibacteriennes, Ph.D Thesis, Ibn Tofail University, 2018 (in French), https://theses.hal.science/tel-03034717.
[54] C. Liu, Y. Huang, W. Shen, J. Cui, Kinetics of hydroxyapatite precipitation at pH 10 to 11, Biomater 22 (2001) 301–306, https://doi.org/10.1016/S0142-9612(00)00166-6.

[55] S. Raynaud, E. Champion, D. Bernache-Assollant, Calcium phosphate apatites with variable Ca/P atomic ratio II. Calcination and sintering, Biomater 23 (2002) 1073–1080, https://doi.org/10.1016/S0142-9612(01)00219-8.

[56] L. Galea, M. Bohner, J. Thuering, N. Doebelin, C.G. Aneziris, T. Graule, Control of the size, shape and composition of highly uniform, non-agglomerated, sub-micrometer β-tricalcium phosphate and dicalcium phosphate platelets, Biomater 34 (2013) 6388–6401, https://doi.org/10.1016/j.biomaterials.2013.05.026.

[57] A. Destainville, E. Champion, D. Bernache-Assolant, E. Laborde, Synthesis, characterization and thermal behavior of apatitic tricalcium phosphate, Mater. Chem. Phys. 80 (2003) 269–277, https://doi.org/10.1016/S0254-0584(02)00466-2.

[58] M. Bohner, B.L.G. Santoni, N. Döbelin, β-tricalcium phosphate for bone substitution: synthesis and properties, Acta Biomater. 113 (2020) 23–41, https://doi.org/10.1016/j.actbio.2020.06.022.

[59] M. Bohner, T.J. Brunner, N. Doebelin, R. Tang, W.J. Stark, Effect of thermal treatments on the reactivity of nanosized tricalcium phosphate powders, J. Mater. Chem. 18 (2008) 4460–4467, https://doi.org/10.1039/b804314k.

[60] Z. Li, C. Chanéac, G. Berger, S. Delaunay, A. Graff, G. Lefèvre, Mechanism and kinetics of magnetite oxidation under hydrothermal conditions, RSC Adv. 9 (2019) 33633–33642, https://doi.org/10.1039/c9ra03234g.

[61] R.M. Cornell, U. Schwertmann, The Iron Oxides: Structure, Properties, Reactions, Occurences and Uses, Wiley, New Jersey, 2003, https://doi.org/10.1002/3527602097 first ed.

[62] K. Witte, W. Bodnar, N. Schell, G. Fulda, E. Burkel, Phase transformations of stoichiometric mixtures of hematite and iron under FAST conditions, J. Alloys Compd. 724 (2017) 728–734, https://doi.org/10.1016/j.jallcom.2017.07.089.

[63] J.R. Morales, J.E. Garay, M. Biasini, W.P. Beyermann, Magnetic characterization of bulk nanostructured iron oxides, Appl. Phys. Lett. 93 (2008) 022511, https://doi.org/10.1063/1.2959070.

[64] J.R. Morales, S. Tanju, W.P. Beyermann, J.E. Garay, Exchange bias in large three dimensional iron oxide nanocomposites, Appl. Phys. Lett. 96 (2010) 013102, https://doi.org/10.1063/1.3277147.

[65] N. Döbelin, Interlaboratory study on the quantification of calcium phosphate phases by Rietveld refinement, Powder Diffr. 30 (2015) 231–241, https://doi.org/10.1017/S088571561500038X.

[66] D. Arcos, J. Rodríguez-Carvajal, M. Vallet-Regí, The effect of the silicon incorporation on the hydroxylapatite structure. A neutron diffraction study, Solid. State Sci. 6 (2004) 987–994, https://doi.org/10.1016/j.solidstatesciences.2004.05.001.

[67] S. Nicolopoulos, J.M. González-Calbet, M.P. Alonso, M.T. Gutierrez-Ríos, M.I. de Frutos, M. Vallet-Regí, Characterization by TEM of local crystalline changes during irradiation damage of hydroxyapatite compounds, J. Solid State Chem. 116 (1995) 265274, https://doi.org/10.1006/jssc.1995.1212.

[68] H.R. Low, N. Phonthammachai, A. Maignan, G.A. Stewart, T.J. Bastow, L.L. Ma, T.J. White, The crystal chemistry of ferric oxyhydroxyapatite, Inorg. Chem. 47 (2008) 11774–11782, https://doi.org/10.1021/ic801491t [64].

[69] L. Pluduma, K.A. Gross, C. Rey, A. Ubelis, A. Berzina, Production and characterization of oxyhydroxyapatites, Key Eng. Mater. 762 (2018) 48–53, https://doi.org/10.4028/www.scientific.net/KEM.762.48.

[70] B. Owusu Asimeng, D. Walter Afeke, E.Kwason Tiburu, Biomaterial for bone and dental implants: synthesis of B-type carbonated hydroxyapatite from biogenic source, in: P. Vizureanu, C.M.C.F. Botelho (Eds.), Biomaterials, IntechOpen, United Kingdom, 2020, p. 92256, https://doi.org/10.5772/intechopen.92256.

[71] L. Berzina-Cimdina, N. Borodajenko, Research of calcium phosphates using fourier transform infrared spectroscopy, in: T. Theophanides (Ed.), Infrared Spectroscopy - Materials Science, Engineering and Technology, IntechOpen, United Kingdom, 2012, pp. 123–148, https://doi.org/10.5772/36942.

[72] S. Meejoo, W. Maneeprakorn, P. Winotai, Phase and thermal stability of nanocrystalline hydroxyapatite prepared via microwave heating, Thermochim. Acta 447 (2006) 115–120, https://doi.org/10.1016/j.tca.2006.04.013.

[73] V. Zheltova, A. Vlasova, N. Bobrysheva, I. Abdullin, V. Semenov, M. Osmolowsky, M. Voznesenskiy, O. Osmolovskaya, Fe_3O_4@HAp core–shell nanoparticles as MRI contrast agent: Synthesis, characterization and theoretical and experimental study of shell impact on magnetic properties, Appl. Surf. Sci. 531 (2020) 147352, https://doi.org/10.1016/j.apsusc.2020.147352.

[74] V.S. Chandra, G. Baskar, R.V. Suganthi, K. Elayaraja, M.I.A. Joshy, W.S. Beaula, R. Mythili, G. Venkatraman, S.N. Kalkura, Blood compatibility of iron-doped nanosize hydroxyapatite and its drug release, ACS Appl. Mater. Interf. 4 (2012) 1200–1210, https://doi.org/10.1021/am300140q.

[75] M. Gotić, S. Musić, Mössbauer, FT-IR and FE SEM investigation of iron oxides precipitated from $FeSO_4$ solutions, J. Mol. Struct. (2007) 445–453, https://doi.org/10.1016/j.molstruc.2006.10.059, 834–836.

[76] A. Radoń, A. Drygała, Ł. Hawełek, D. Łukowiec, Structure and optical properties of Fe_3O_4 nanoparticles synthesized by co-precipitation method with different organic modifiers, Mater. Charact. 131 (2017) 148–156, https://doi.org/10.1016/j.matchar.2017.06.034.

[77] S. Nasrazadani, A. Raman, The application of infrared spectroscopy to the study of rust systems-II. Study of cation deficiency in magnetite (Fe_3O_4) produced during its transformation to maghemite (γ-Fe_2O_3) and hematite (α-Fe_2O_3), Corr. Sci. 34 (1993) 1355–1365, https://doi.org/10.1016/0010-938X(93)90092-U.

[78] M. Nazari, N. Ghasemi, H. Maddah, M.M. Motlagh, Synthesis and characterization of maghemite nanopowders by chemical precipitation method, J. Nanostruc. Chem. 4 (2014) 99, https://doi.org/10.1007/s40097-014-0099-9.

[79] A.G. Roca, J.F. Marco, M. Del Puerto Morales, C.J. Serna, Effect of nature and particle size on properties of uniform magnetite and maghemite nanoparticles, J. Phys. Chem. C 111 (2007) 18577–18584, https://doi.org/10.1021/jp075133m.

[80] V. Iannotti, A. Adamiano, G. Ausanio, L. Lanotte, G. Aquilanti, J.M.D. Coey, M. Lantieri, G. Spina, M. Fittipaldi, G. Margaris, Fe-doping-induced magnetism in nano-hydroxyapatites, ACS Inorg. Chem. 56 (2017) 4446–4458, https://doi.org/10.1021/acs.inorgchem.6b03143.

[81] F. Ren, Y. Ding, Y. Leng, Infrared spectroscopic characterization of carbonated apatite: a combined experimental and computational study, J. Biomed. Mater. Res. A 102 (2014) 496–505, https://doi.org/10.1002/jbm.a.34720.

[82] F. Ren, Y. Leng, Carbonated apatite, Type-A or Type-B? Key Eng. Mater. (2012) 293–297, https://doi.org/10.4028/www.scientific.net/KEM.493-494.293, 493-494.

[83] H. Namduri, S. Nasrazadani, Quantitative analysis of iron oxides using Fourier transform infrared spectrophotometry, Corros. Sci. 50 (2008) 2493–2497, https://doi.org/10.1016/j.corsci.2008.06.034.

[84] M. Stoia, R. Istratie, C. Păcurariu, Investigation of magnetite nanoparticles stability in air by thermal analysis and FTIR spectroscopy, J. Therm. Anal Calorim. 125 (2016) 11851198, https://doi.org/10.1007/s10973-016-5393-y.

[85] K.G. Gareev, Diversity of iron oxides: mechanisms of formation, physical properties and applications, Magnetochemistry 9 (2023) 119, https://doi.org/10.3390/magnetochemistry9050119.

[86] N.V. Bulina, S.V. Makarova, S.G. Baev, A.A. Matvienko, K.B. Gerasimov, O. A. Logutenko, V.S. Bystrov, A study of thermal stability of hydroxyapatite, Minerals 11 (2021) 1310, https://doi.org/10.3390/min11121310.

[87] K. Tõnsuaadu, K.A. Gross, L. Plūduma, M. Veiderma, A review on the thermal stability of calcium apatites, J. Therm. Anal. Calorim. 110 (2012) 647–659, https://doi.org/10.1007/s10973-011-1877-y.

[88] F. Pupilli, M. Tavoni, C. Drouet, A. Tampieri, S. Sprio, Iron-doped hydroxyapatite by hydrothermal synthesis: Factors modulating the Fe^{2+}, Fe^{3+} content, Open Ceramics 18 (2024) 100610, https://doi.org/10.1016/j.oceram.2024.100610.

[89] S.V. Makarova, N.V. Bulina, O.B. Vinokurova, A.V. Ishchenko, Thermal stability of iron- and silicon-substituted hydroxyapatite prepared by mechanochemical method, Powders 2 (2023) 372–386, https://doi.org/10.3390/powders2020022.

[90] Z. Klencsár, A. Ábrahám, L. Szabó, E.G. Szabó, S. Stichleutner, E. Kuzmann, Z. Homonnay, G. Tolnai, The effect of preparation conditions on magnetite nanoparticles obtained via chemical co-precipitation, Mater. Chem. Phys. 223 (2019) 122–132, https://doi.org/10.1016/j.matchemphys.2018.10.049.

[91] R. Hergt, S. Dutz, M. Röder, Effects of size distribution on hysteresis losses of magnetic nanoparticles for hyperthermia, 2008. *J. of Phys. Cond. Matter.* 20, 385214. https://doi.org/10.1088/0953-8984/20/38/385214. [84]E. F. Kneller, F. E. Luborsky, Particle size dependence of coercivity and remanence of single-domain particles, *J. Appl. Phys*. 34 (1963) 656–658. https://doi.org/10.1063/1.1729324.

[92] C.R. Kalaiselvan, S.S. Laha, S.B. Somvanshi, T.A. Tabish, N.D. Thorat, N.K. Sahu, Manganese ferrite ($MnFe_2O_4$) nanostructures for cancer theranostics, Coord. Chem. Rev. 473 (2022) 214809, https://doi.org/10.1016/j.ccr.2022.214809.

[93] H. Gavilán, K. Simeonidis, E. Myrovali, O. Chubykalo-Fesenko, R. Chantrell, L. Balcells, M. Angelakeris, M.P. Morales, D. Serantes, How size, shape and assembly of magnetic nanoparticles give rise to different hyperthermia scenarios, Nanoscale 13 (2021) 1563115646, https://doi.org/10.1039/d1nr03484g.

[94] Y. Lv, Y. Yang, J. Fang, H. Zhang, E. Peng, X. Liu, W. Xiao, J. Ding, Size dependent magnetic hyperthermia of octahedral Fe_3O_4 nanoparticles, RSC Adv. 5 (2015) 7676476771, https://doi.org/10.1039/c5ra12558h.

[95] O.L. Lanier, O.I. Korotych, A.G. Monsalve, D. Wable, S. Savliwala, N.W. F. Grooms, C. Nacea, O.R. Tuitt, J. Dobson, Evaluation of magnetic nanoparticles for magnetic fluid hyperthermia, Intern. J. Hyperthermia 36 (2019) 687–701, https://doi.org/10.1080/02656736.2019.1628313.

[96] O. Szasz, G. Szigeti, A. Szasz, Connections between the specific absorption rate and the local temperature, Open J. Biophys. 06 (2016) 53–74, https://doi.org/10.4236/ojbiphy.2016.63007.

[97] R.R. Wildeboer, P. Southern, Q.A. Pankhurst, On the reliable measurement of specific absorption rates and intrinsic loss parameters in magnetic hyperthermia materials, J. Phys. D Appl. Phys. 47 (2014) 687–701, https://doi.org/10.1088/0022-3727/47/49/495003.

[98] I. Andreu, E. Natividad, Accuracy of available methods for quantifying the heat power generation of nanoparticles for magnetic hyperthermia, Intern. J. of Hyperthermia 29 (2013) 739–751, https://doi.org/10.3109/02656736.2013.826825.

[99] E. Garaio, O. Sandre, J.M. Collantes, J.A. Garcia, S. Mornet, F. Plazaola, Specific absorption rate dependence on temperature in magnetic field hyperthermia measured by dynamic hysteresis losses (AC magnetometry), Nanotechnology 26 (2015) 015704, https://doi.org/10.1088/0957-4484/26/1/015704.

[100] S.B. Somvanshi, S.R. Patade, D.D. Andhare, S.A. Jadhav, M.V. Khedkar, P. B. Kharat, P.P. Khirade, K.M. Jadhav, Hyperthermic evaluation of oleic acid coated nano-spinel magnesium ferrite: Enhancement via hydrophobic-to-hydrophilic surface transformation, J. Alloys Compd. 835 (2020) 155422, https://doi.org/10.1016/j.jallcom.2020.155422.

[101] J. Motoyama, T. Hakata, R. Kato, N. Yamashita, T. Morino, T. Kobayashi, H. Honda, Size dependent heat generation of magnetite nanoparticles under AC magnetic field for cancer therapy, Biomagn. Res. Technol. 6 (2008) 4, https://doi.org/10.1186/1477-044X-6-4.

[102] S.B. Somvanshi, S.A. Jadhav, S.S. Gawali, K. Zakde, K.M. Jadhav, Core-shell structured superparamagnetic Zn-Mg ferrite nanoparticles for magnetic hyperthermia applications, J. Alloys Compd. 947 (2023) 169574, https://doi.org/10.1016/j.jallcom.2023.169574.